

Therapeutic application of circular RNA aptamers in a mouse model of psoriasis

Received: 20 October 2023

Accepted: 12 March 2024

Published online: 23 April 2024

 Check for updates

Si-Kun Guo^{1,9}, Chu-Xiao Liu^{1,9}, Yi-Feng Xu^{1,9}, Xiao Wang^{1,9}, Fang Nan^{2,9}, Youkui Huang¹, Siqi Li¹, Shan Nan¹, Ling Li^{1,3}, Edo Kon⁴, Chen Li¹, Meng-Yuan Wei¹, Rina Su⁵, Jia Wei², Shiguang Peng⁵, Nitay Ad-El⁴, Jiaquan Liu¹, Dan Peer⁴, Ting Chen⁶, Li Yang² & Ling-Ling Chen^{1,3,7,8} ✉

Efforts to advance RNA aptamers as a new therapeutic modality have been limited by their susceptibility to degradation and immunogenicity. In a previous study, we demonstrated synthesized short double-stranded region-containing circular RNAs (ds-cRNAs) with minimal immunogenicity targeted to dsRNA-activated protein kinase R (PKR). Here we test the therapeutic potential of ds-cRNAs in a mouse model of imiquimod-induced psoriasis. We find that genetic supplementation of ds-cRNAs leads to inhibition of PKR, resulting in alleviation of downstream interferon- α and dsRNA signals and attenuation of psoriasis phenotypes. Delivery of ds-cRNAs by lipid nanoparticles to the spleen attenuates PKR activity in examined splenocytes, resulting in reduced epidermal thickness. These findings suggest that ds-cRNAs represent a promising approach to mitigate excessive PKR activation for therapeutic purposes.

Several RNA-based drug modalities have received regulatory approval, including small interfering RNAs, antisense oligonucleotides, mRNA vaccines and RNA aptamers^{1,2}. Compared to other categories of RNA drugs, RNA aptamers face greater challenges owing to their susceptibility to RNase enzymes and their immunogenicity, as well as poorly defined mechanisms of action. Covalently closed circular RNAs (circRNAs) have been shown to offer high stability^{3,4}, unique conformation^{5,6} and low immunogenicity^{7,8}, compared to linear RNAs, offering great pharmaceutical potential⁹.

Overactivation of double-stranded RNA (dsRNA)-activated protein kinase R (PKR) is linked to auto-inflammatory diseases^{10–14},

such as systemic lupus erythematosus (SLE)⁶, suggesting that blocking PKR activation holds therapeutic promise for such diseases. While chemical inhibitors of PKR suffer from off-target effects and reduced *in vivo* activity^{15–17}, modulating PKR activity can be achieved by RNA duplexes¹⁰, such as short double-stranded region-containing circular RNAs (ds-cRNAs) via ectopic plasmids in SLE-derived peripheral blood mononuclear cells (PBMCs)⁶, and synthesized ds-cRNAs with low immunogenicity in cultured cells⁸.

Psoriasis, a chronic papulosquamous skin disease, primarily presents as chronic plaque or psoriasis vulgaris¹⁸. Reduced expression of endogenous circRNAs was observed in PBMCs from patients

¹Key Laboratory of RNA Innovation, Science and Engineering, CAS Center for Excellence in Molecular Cell Science, Shanghai Institute of Biochemistry and Cell Biology, University of Chinese Academy of Sciences, Chinese Academy of Sciences, Shanghai, China. ²Center for Molecular Medicine, Children's Hospital of Fudan University and Shanghai Key Laboratory of Medical Epigenetics, International Laboratory of Medical Epigenetics and Metabolism, Ministry of Science and Technology, Institutes of Biomedical Sciences, Fudan University, Shanghai, China. ³School of Life Science and Technology, ShanghaiTech University, Shanghai, China. ⁴Laboratory of Precision Nanomedicine, Shmunis School of Biomedicine and Cancer Research, George S. Wise Faculty of Life Sciences, Department of Materials Sciences and Engineering, Iby and Aladar Fleischman Faculty of Engineering, Center for Nanoscience and Nanotechnology, Cancer Biology Research Center, Tel Aviv University, Tel Aviv, Israel. ⁵Department of Dermatology, Beijing Chao-yang Hospital, Capital Medical University, Beijing, China. ⁶National Institute of Biological Sciences, Tsinghua Institute of Multidisciplinary Biomedical Research, Tsinghua University, Beijing, China. ⁷New Cornerstone Science Laboratory, Shenzhen, China. ⁸Key Laboratory of Systems Health Science of Zhejiang Province, School of Life Science, Hangzhou Institute for Advanced Study, University of Chinese Academy of Sciences, Hangzhou, China. ⁹These authors contributed equally: Si-Kun Guo, Chu-Xiao Liu, Yi-Feng Xu, Xiao Wang, Fang Nan. ✉e-mail: linglingchen@sibcb.ac.cn

with lupus⁶ and in lesional skin affected by chronic inflammatory skin diseases such as psoriasis and atopic dermatitis^{19–21}. These observations have prompted us to investigate the connection between reduced circRNAs and increased inflammation, and to explore whether ds-cRNAs can suppress the hyperactive PKR-related inflammation in psoriatic mice.

Here we optimized a user-friendly permuted-intron–exon (PIE) strategy to produce RNA circles with high yield and low immunogenicity. Such ds-cRNAs with high binding capacity to PKR can alleviate inflammation by attenuating pathological PKR activity in an imiquimod (IMQ)-induced psoriasis mouse model²², representing RNA aptamers with therapeutic potential.

Results

Optimized PIE for circRNA synthesis

RNA circles produced via direct ligation with a few extraneous nucleotides showed little cellular immunogenicity, but efficiency of this method depend on length and structure of precursor sequences²³, and could be limited for long sequences without additional effort on termini proximity⁸. The PIE strategy derived from group I autocatalytic introns can produce RNA circles with high efficiency; however, extraneous fragments introduced by PIE often fold into distorted circular structures, provoking innate immune responses⁸. As PIE had advantages in yield, we sought to optimize it to produce scalable and low immunogenic RNA circles.

We generated *Anabaena* transfer RNA (tRNA)^{Leu}-derived PIE with varied lengths of extraneous nucleotides, including reported 66 nucleotides (nt) (ref. 24) and 186 nt (ref. 25) where each contains an additional spacer to form a long duplex at the junction site to promote circularization, and five shorter versions (Fig. 1a). In silico secondary structure prediction showed a clover-like structure for the 49 nt, a dumbbell-like structure for the 41 nt, a stem-loop from the anticodon arm of tRNA^{Leu} for the 27 nt and a single-stranded region for 13 and 7 nt versions that might interfere with adjacent sequences (Fig. 1b).

We tested their circularization capability for short (the human circPOLR2A(9,10), 336 nt) and long (internal ribosome entry site (IRES)-mCherry, 1,452 nt) cargos individually (Fig. 1c and Extended Data Fig. 1a). Denaturing polyacrylamide gel electrophoresis (PAGE) of each sample produced by in vitro transcription (IVT), circularization and RNase R digestion revealed that the extraneous 27 nt in PIE showed a high efficiency in circularizing many RNAs (Fig. 1c and Extended Data Fig. 1a), with a size up to roughly 7,000 nt (Fig. 1d), suggesting its generality in producing RNA circles. In silico structure prediction showed that the 27 nt tended to form a 5 basepair (bp) strong pairing stem and a 7 nt loop at the junction site (Extended Data Fig. 1b), which appeared to be sufficient for circularization. This was confirmed by selective 2'-hydroxyl acylation analyzed by primer extension and mutational profiling for circRNAs (circSHAPE-MaP) with 2-methylnicotinic acid

imidazolide (NAI) for secondary conformation^{8,26}. The 27 nt extraneous sequence alone formed a stable stem-loop at the junction site, barely interfering with examined cargo sequences (Extended Data Fig. 1b). By contrast, the 13 and 7 nt versions were unlikely to form a pair (Fig. 1b) and failed to efficiently produce RNA circles (Fig. 1c and Extended Data Fig. 1a). Notably, unlike PIE with long stretches of extraneous nucleotides (186 or 66 nt), RNA circles generated by the 27 nt version minimally triggered expression of transcripts for inflammatory factors such as IFN β , IL6, TNF α or RIG-I in A549 cells (Extended Data Fig. 1c). Altogether, the 27 nt version PIE represents an efficient approach to circularize RNA with little immunogenicity. We thereafter named it Ana_PIE_27nt for simplicity.

Increased yield and efficacy of ds-cRNAs as PKR inhibitors

As an effective RNA aptamer requires a desired conformation for functions, we aimed to design a junction site to avoid dsRNA structural distortion in the RNA circle. circPOLR2A_Lig, synthesized by direct ligation, could form desired imperfect duplexes to inhibit PKR activation⁸. To make a potent ds-cRNA aptamer by PIE resembling circPOLR2A_Lig, we designed the junction site located at the distal single-stranded region, resulting in circPOLR2A_J (Extended Data Fig. 1d). The original junction site of circPOLR2A_Lig (ref. 8), which was located in the imperfect duplex region (Extended Data Fig. 1d), was included for self-splicing to produce circPOLR2A_Ana_27nt as a control.

These different ds-cRNAs generated by Ana_PIE_27nt were tested for their inhibitory effects on PKR activation (phosphorylated PKR, p-PKR), stimulated by 79 bp dsRNA in vitro (Fig. 1e and Extended Data Fig. 1e,f). CircPOLR2A_J displayed the most potent inhibitory effect on PKR activation (Fig. 1e), indicating that circPOLR2A_J folds into the most desired conformation to suppress PKR activation. Of note, neither the linear form of POLR2A (Fig. 1e) nor a circle of 27 nt extraneous nucleotides alone (Extended Data Fig. 1f) could suppress PKR phosphorylation. Given that PKR is conserved^{27,28}, circPOLR2A_J also showed a remarkably inhibition on mouse p-Pkr (Extended Data Fig. 1g). Consistently, aligning the minimum free energy of the predicted secondary structure showed that circPOLR2A_J was more stable than circPOLR2A_Lig (Extended Data Fig. 1d). We hereafter named circPOLR2A_J as efficient PKR inhibitor ds-cRNA (EPIC).

The low yield of circPOLR2A_Lig was due to extra guanosine monophosphates added during transcription for 5' end priming, and limited circularization capability by the competition of intermolecular ligation⁸. By contrast, EPIC production had advantages in transcription and time-saving self-splicing (Fig. 1f). Analyzing yields of EPIC and circPOLR2A_Lig purified under the same procedure, in which linear RNAs were removed by RNase R followed by the alkaline phosphatase treatment to reduce traceable immunogenicity, showed that EPIC was about tenfold higher in yield than circPOLR2A_Lig (Fig. 1g). Transfection of EPIC was unable to induce significant expression of

Fig. 1 | Synthesized ds-cRNA (EPIC) via an engineered circularization strategy prevents PKR activation. **a**, Schematic illustration of the circularization strategy based on the permuted *Anabaena* group I intron^{24,25} optimized with truncated extraneous sequences. Blue, sequences to be circularized; coral, 3' extraneous nucleotides from exon 1 (E1); green, 5' extraneous nucleotides from exon 2 (E2); gray, catalytic intron. **b**, In silico secondary structure prediction of different extraneous nucleotides. Blue and yellow shadows indicate 5' and 3' extraneous nucleotides in Ana_PIE_27nt, respectively. **c**, The 27 nt extraneous sequence (Ana_PIE_27nt) is sufficient to improve circularization for both short and long cargos. Circularized RNA products are analyzed with PAGE (Extended Data Fig. 1a) and quantified with ImageJ. Data are shown as dots and means connected with lines from three replicates. **d**, Ana_PIE_27nt can efficiently produce different circular cargos with the examined size up to roughly 7,000 nt. Circularized RNA products are analyzed with denaturing PAGE, except *, with agarose gel. Bands of RNA circles are verified with RNase R and marked with blue arrows. **e**, Engineered ds-cRNA suppresses p-PKR efficiently. Purified PKR (0.6 μ M) is activated by 79 bp

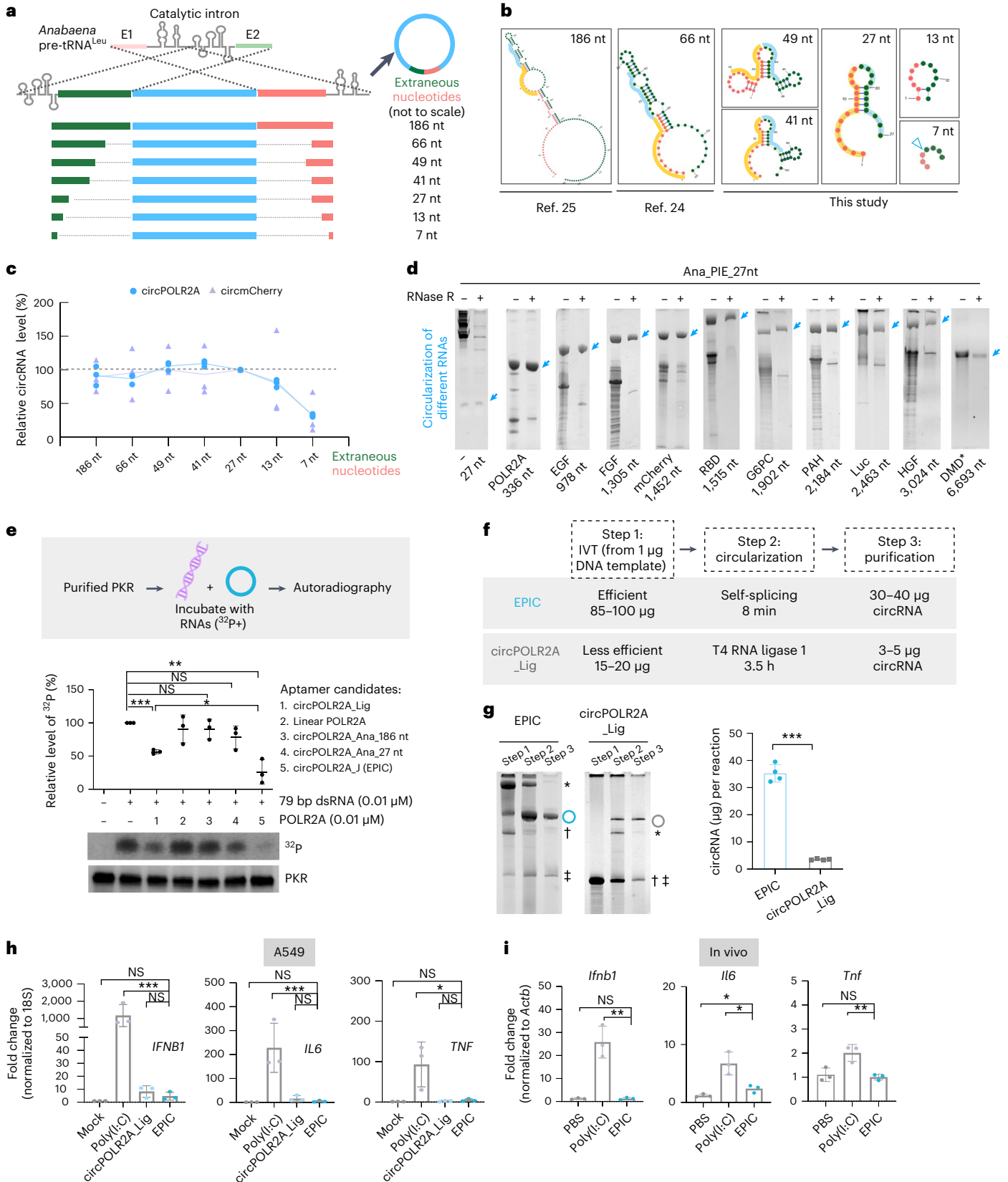
dsRNA (0.01 μ M) in vitro, shown by autoradiography using [γ -³²P]ATP. 0.01 μ M of each POLR2A-derived aptamer candidate is used. **f**, A comparison of the key steps and their performance in the two RNA circularization strategies. **g**, Products of each step shown in **f**, are analyzed by denaturing PAGE and quantified by spectrophotometry. Quantification for the yield of each reaction is shown in right from four replicates. The hollow circles are RNA circles; single daggers, linear precursors; double daggers, nicked circles; asterisks, concatenations. **h**, EPIC did not induce inflammatory cytokines in cells. Relative expression of inflammatory cytokines after 6 hours of transfection are measured by RT-qPCR, normalized to expression of mock transfection. **i**, EPIC did not induce inflammatory cytokines in vivo. The same amounts of EPIC and control RNAs (1 μ g for each sample) were delivered by LNPs into mice spleens ($n = 3$). Relative expression of inflammatory cytokines in mice spleen cells after 6 hours of delivery are measured by RT-qPCR, normalized to expression of PBS treatment. **e, g–i**, not significant (NS) $P > 0.05$, * $P < 0.05$, ** $P < 0.005$, *** $P < 0.001$, two-tailed Student's t -test, data are shown as mean \pm standard deviation (s.d.).

inflammatory cytokines in A549 cells (Fig. 1h), nor by in vivo delivery by lipid nanoparticles (LNPs, also Fig. 4) into mice (Fig. 1i).

Robust binding of ds-cRNA to PKR in solution

Possessing a high specificity for target binding is an essential criterion of a therapeutic aptamer. circPOLR2A_Lig showed a 1,000-fold higher

inhibitory effect than ATP-binding site-directed small molecules on PKR activation⁸; EPIC showed an even higher suppressive effect than circPOLR2A_Lig on long dsRNA-stimulated PKR activity (Fig. 1e). To address how circular aptamers achieve the potent suppression of p-PKR, we used single-molecule total internal reflection fluorescence (smTIRF) microscopy to observe dynamic PKR–RNA interactions^{29,30}.



We synthesized 79 bp dsRNA (PKR activator), 33 bp dsRNA (PKR inhibitor), EPIC and an RNA circle lacking a duplex region (non-ds-cRNA, circSMARCA5), which were labeled with Cy5 and biotin simultaneously. The labeling had no apparent impact on EPIC conformation, shown by similar SHAPE signals between labeled and unlabeled EPICs (Extended Data Fig. 2a). Labeled RNAs were immobilized on a quartz surface coated with PEG-biotin through biotin–neutravidin interactions. Single RNA molecules were then recorded, followed by PKR–Cy3 injection. This allowed us to visualize dynamics of PKR on distinct RNA–Cy5 substrates (Fig. 2a).

Numerous PKR molecules were colocalized with dsRNAs or EPIC, whereas the colocalization between PKR and circSMARCA5 was barely detected (Fig. 2b and Extended Data Fig. 2b), showing that PKR bound to both dsRNAs and EPIC, but not non-ds-cRNA. Two versions of linear RNA substrate harboring the 23 bp imperfect duplex from EPIC were also generated as a 73 nt hairpin bearing a flexible linker and a 23 bp imperfect duplex alone (Fig. 2c). Notably, smTIRF assays revealed that both substrates copied the transient binding pattern of 79 or 33 bp dsRNAs (Fig. 2d), highlighting the unique property of EPIC in a circular conformation.

Further investigation into PKR–RNA association revealed that the binding of PKR to EPIC was robust, characterized by mostly ‘stable-binding events’ (binding time >120 s, 75.9%) than the 79 bp (20.7%), 33 bp (19.2%), 73 nt hairpin (18.6%) or 23 bp imperfect duplex (12.3%) (Fig. 2e). To compare the stability of RNA-bound PKR, a wash step was introduced after PKR injection to prevent proteins from rebinding (Fig. 2f). Survival probability analyses showed that PKR displayed a much longer lifetime on the single EPIC molecule than those on the linear dsRNA molecule (Fig. 2f,g). Consistently, a similar robust binding was observed between PKR and another ds-cRNA, circCAMSAP1 (ref. 8) (Extended Data Fig. 2c). Thus, ds-cRNAs effectively hindered PKR activation likely due to their strong binding capability, and the tertiary structure within the ds-cRNA appears essential for this stable binding.

Tertiary conformation of ds-cRNA enables specificity for PKR

As the intensity of PKR–Cy3 on the single EPIC molecule was progressively increased (Fig. 2b), we speculated that one EPIC might associate with more than one PKR. To examine this hypothesis, we used single-molecule photobleaching analysis to determine protein stoichiometry³¹. As single-step photobleaching is indicative of a single emitter, such as a monomer, counting the bleaching steps provides a direct way for measuring the quantity of labeled proteins. A hidden Markov model³² was developed for the unbiased analysis of single-molecule data to obtain step information (Extended Data Fig. 2d). Frequency distribution showed that the number of PKR–Cy3 bleaching steps on the single EPIC ranged from 1 to 8 (Fig. 2h), consistent with the increased progressive binding of PKR to EPIC.

As PKR contains an intrinsically disordered region (IDR) between its RNA binding domain and kinase domain³³ (Extended Data Fig. 2e), such an IDR may lead to multivalent colocalization of PKR in solution where a single EPIC binds to multiple PKR molecules, resulting in a nonlinear binding pattern (Fig. 2h). We tested this idea by replacing wild-type (WT) PKR with the PKR IDR truncation (Δ IDR) in smTIRF system (Extended Data Fig. 2e). The interactions between EPIC and PKR- Δ IDR were similar to WT PKR (Extended Data Fig. 2e), excluding the possibility that PKR could phase separate with EPIC.

Next, we attempted to build a three-dimensional (3D) model of how PKR binds to EPIC based on the secondary conformation via circSHAPE–MaP with or without PKR binding. circSHAPE–MaP showed that most nucleotides within EPIC exhibited similar SHAPE reactivities on PKR addition as those in EPIC alone, except five adjoining loops (pink) (Extended Data Fig. 3a,b). Illustrating the predicted EPIC folding accordingly, the imperfect 23 bp RNA duplex (yellow) is located in a central flexible region connecting distal stem loops

(Extended Data Fig. 3a,b). This setting is sufficient for PKR binding. Of note, the length of distal stem loops did not meet the RNA duplex binding criteria of monomeric PKR³⁴ (Extended Data Fig. 3b).

As PKR binding would influence NAI accessibility in nearby regions, altered SHAPE reactivities in these distal loop regions suggested their spatial proximity to the predicted RNA duplex bound by PKR (Extended Data Fig. 3a,b). Results of PKR–Cy3 bleaching steps analysis indicated that each EPIC molecule prefers to bind two PKR molecules (Fig. 2h). Next, we tried to simulate the binding mode of EPIC with two AlphaFold2-predicted PKR molecules (Extended Data Fig. 3c) by the lowest docking score using HDOCK³⁵. PKR binding modes achieved lower ‘lowest docking scores’ on EPIC than on the 79 bp dsRNA (Extended Data Fig. 3c), consistent with the robust suppression of EPIC on PKR activation mediated by the 79 bp dsRNA (Fig. 1e). While two PKR molecules preferred to dock on the 23 bp RNA duplex of EPIC with an antiparallel direction (Extended Data Fig. 3c), likely preventing their kinase domains from forming an activated configuration^{33,36,37}. However, we cannot exclude the possibility that additional PKR may bind loosely to distal stem loops, resulting in altered NAI accessible regions (Extended Data Fig. 3a,b).

Dysregulated circRNA–PKR axis in psoriasis mice

A dysregulated RNase L–circRNA–PKR axis was found in SLE patient-derived cells⁶. Given that SLE is one of the most heterogeneous autoinflammation disorders^{38,39}, we sought to explore a less complicated model featuring dysregulated RNase L–circRNA–PKR axis to evaluate the therapeutic potent of ds-cRNAs in vivo.

Daily administration of IMQ at day (D) 0, 1, 2, 3, 5 and 8 onto the back skin of mice induces inflamed scaly skin lesions resembling plaque-type psoriasis, representing a classic model with most features of human psoriasis^{22,40} (Extended Data Fig. 4a). Reported spleen enlargement^{22,40} was observed starting on D2, and reached a peak on D5 (Extended Data Fig. 4a). Given the frequent occurrence of systemic inflammatory defects of psoriasis, we opted to use the ds-cRNA treatment by targeting spleen.

Total RNAs of spleens in mice treated with IMQ at different days were collected (Fig. 3a). An increased expression of psoriasis-related *Il17a* and *Il23a* mRNAs on D5 (Extended Data Fig. 4b) was consistent with a previous report²², supporting the feasibility of using splenocytes for investigating psoriasis pathogenesis. We also observed expression of *Pkr* and *Il6* (Extended Data Fig. 4b), along with RNase L activation, peaking on D1 (Extended Data Fig. 4c). Correspondingly, dramatically increased PKR levels on D1 and D2 and p-PKR from D2 to D5 were observed (Fig. 3b), suggesting that transient *Pkr* expression could result in prolonged PKR phosphorylation and cascade downstream inflammatory effects mediated by PKR activation⁴¹. Of note, the elevated expression of these fast-responding genes corresponded to the increased thickness of interfollicular epidermis initiated on D1 and reaching a plateau on D2 (Extended Data Fig. 4d). Thus, blocking PKR activation, in principle, may mitigate psoriasis progression.

Consistent with transient RNase L activation (Extended Data Fig. 4c), analysis of the ribosomal RNA (rRNA)-depleted RNA sequencing (RNA-seq) of psoriatic spleens via CIRCexplorer⁴² revealed a greater global reduction of circRNAs than linear RNAs on IMQ (Fig. 3c and Extended Data Fig. 4e,f). Collectively, these analyses suggested a previously uncharacterized dysregulated RNase L–circRNA–PKR axis in psoriatic pathogenesis.

PKR is one fast-responding inflammatory factor in psoriasis mice

Although thickened interfollicular epidermis was initiated on D1 (Extended Data Fig. 4d), currently available transcriptomics of the IMQ mice have only been analyzed on D5 (refs. 22,40), indicating a possible overlook of fast-responding inflammatory factors, such as *Pkr* and *Il6*, during this process (Extended Data Fig. 4b). We thus analyzed

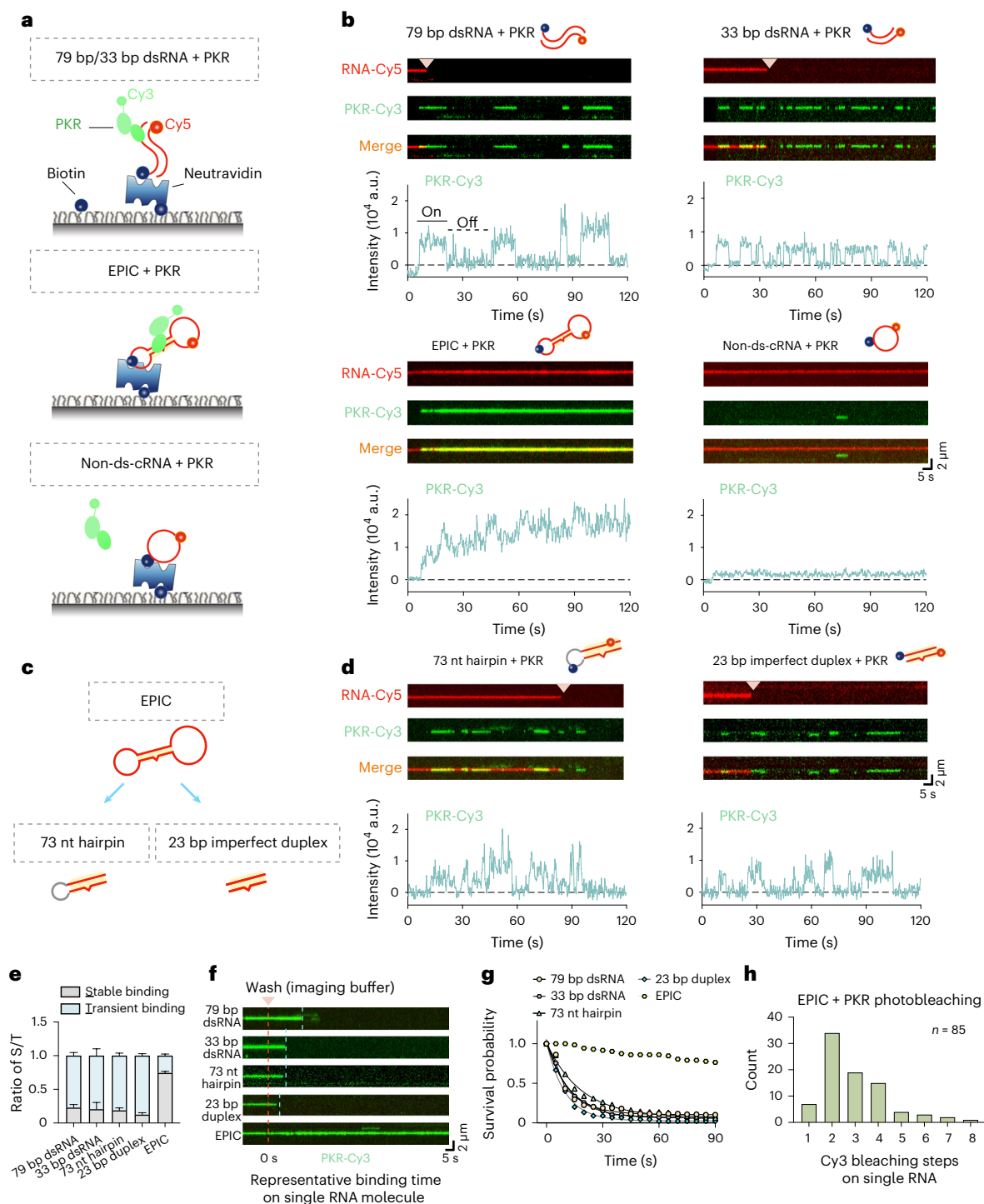


Fig. 2 | The high affinity of EPIC with PKR in dynamics. **a**, Schematic of smTIRF to image direct interactions between PKR and different RNAs. Cy5 and biotin are terminally labeled for linear dsRNAs, but are internally labeled by IVT during circRNA production. After PKR-Cy3 injection, the single-molecule videos in two corresponding channels are recorded. **b**, EPIC interacts with PKR with high affinity compared to linear dsRNAs and the non-ds-cRNA control (circSMARCA5). For each type of RNA, the representative kymographs (top) of RNA-Cy5 binding with PKR-Cy3 are shown in separated and merged channels, and quantifications (bottom) of the PKR-Cy3 intensity on the single RNA molecule within 120 s are shown. Triangles represent Cy5 photobleaching. **c**, The 73 nt hairpin RNA and 23 bp imperfect duplex RNA share the same 23 bp imperfect duplex in EPIC, marked by yellow shadow. **d**, PKR on 73 nt hairpin RNA (internal label) or 23 bp imperfect duplex RNA (terminal label) substrates displays transient binding events. **e**, PKR stably binds EPIC. Relative ratio of stable-binding events (S) versus

transient binding events (T) of each examined RNA substrate is shown. The number of PKR-Cy3 counted in each column with three replicates: 79 bp dsRNA, $n = 133, 74, 89$; 33 bp dsRNA, $n = 48, 35, 26$; 73 nt hairpin RNA, $n = 84, 103, 161$; 23 bp duplex, $n = 20, 32, 36$; EPIC, $n = 27, 32, 63$. Data are shown as mean \pm s.d. **f**, Representative kymographs of PKR survival lifetime measurement on a single RNA substrate. Red dashes represent the injection of the imaging buffer (0 s), blue dashes represent the dissociation of PKR and the intervals between two time points are measured as the survival lifetime of PKR on the single RNA molecule. **g**, Survival probability of the single PKR on examined RNAs. Data are fitted in one phase decay curve: 79 bp dsRNA, $n = 138$; 33 bp dsRNA, $n = 98$; 73 nt hairpin RNA, $n = 130$; 23 bp duplex RNA, $n = 45$; EPIC, $n = 72$. **h**, The number of PKR bindings on a single EPIC molecule is calculated based on the step analysis of photobleaching from single-molecule fluorescence imaging of PKR-Cy3. n , number of events examined.

dynamic transcriptomics along IMQ treatment on mice to discern their possible correlations with psoriatic pathogenesis.

We selected genes with over threefold upregulation on D1 compared to D0 in two biological repeats, and identified 787 differentially expressed genes (DEGs) (Extended Data Fig. 5a). These elevated DEGs on D1 displayed divergent patterns afterwards, which could be grouped into six clusters by Mfuzz^{43,44} (Fig. 3d). PKR was classified into cluster 1 along with 150 others, whose expression was increased remarkably on D1, but declined to the initial D0 level afterwards (Fig. 3d). Kyoto Encyclopedia of Genes and Genomes (KEGG) pathway enrichment analyses showed that the most altered genes of Cluster 1 belonged to the interferon (IFN) α -related genes and dsRNA sensor related pathways (Extended Data Fig. 5b). As IFN α belongs to the type I IFN family, which can activate immature dendritic cells to produce IL-12, IL-15, IL-18 and IL-23 (ref. 45), IFN α has been considered to be one initiator of psoriatic inflammation acting as an upstream cytokine within the psoriatic inflammatory cascades⁴⁶. We thus subclassified these Cluster 1 genes as fast-responding inflammatory factors (Extended Data Fig. 5c).

In terms of the time-course pattern following D1, Cluster 2 genes declined by roughly 70% to a level higher than D0 (Fig. 3d). Cluster 3 genes maintained high expression on D2 and then declined by roughly 75% on D5 (Fig. 3d). A total of 158 genes of Cluster 2 and 112 genes of Cluster 3 were mostly enriched in pathways related to protein translation and metabolism (Extended Data Fig. 5d,e), indicating changes in proteome and cellular homeostasis initiated after the innate immune responses triggered by Cluster 1 genes (Extended Data Fig. 5c). Cluster 4 genes peaked on D2 with about sevenfold upregulation to D0 and declined on D5 (Fig. 3d), and this cluster included 103 genes enriched in pathways of neutrophil formation and SLE pathogenesis (Extended Data Fig. 5f). Cluster 5 plateaued with four- to sixfold upregulation compared to D0, while Cluster 6 genes kept ascending from D1 to D5 (Fig. 3d). Genes in Clusters 5 and 6 were enriched in pathways related to cell cycle, DNA replication and repair, highlighting changes in gene expression in the late-stage pathogenesis related to long-term psoriatic phenotypes including spleen enlargement and epidermal hyperplasia (Extended Data Fig. 5g,h).

PKR modulates the early inflammation in psoriatic pathogenesis

We asked whether such a distinct PKR activation plays a role in psoriatic pathogenesis. We generated PKR-deficient (*Pkr*^{-/-}) mice (Extended Data Fig. 6a), which appeared normal in development compared with WT mice as reported⁴⁷. Treating *Pkr*^{-/-} mice with IMQ as WT mice (Fig. 3a) followed by total RNA-seq of psoriatic spleens revealed that PKR depletion did not affect circRNA levels (Extended Data Fig. 6b) compared with WT samples (Fig. 3c) as expected. Increased expression of fast-responding inflammatory factors on D1 was largely impaired in *Pkr*^{-/-} mice (Fig. 3e and Extended Data Fig. 6c). Given that TLR7 is a key factor in the IMQ model⁴⁰, the decreased *Tlr7* expression in *Pkr*^{-/-} mice

strengthens the role of PKR in IMQ-induced psoriatic pathogenesis (Extended Data Fig. 6c). PKR depletion also mildly affected IL-23/IL-17 expression (Extended Data Fig. 6c): signature genes of late-stage IMQ mice (Extended Data Fig. 4b)⁴⁶. Consistently, reduced epidermis thickness was observed in *Pkr*^{-/-} mice, compared to WT mice, after IMQ treatment (Fig. 3f).

Collectively, our results in splenocytes of the IMQ mice exhibited a general consistency with the context in skin as shown previously⁴⁸⁻⁵⁰. These earlier reports indicated that skin inflammation was triggered by dsRNAs in psoriatic keratinocytes⁵⁰ and that dampened dsRNA sensor pathways could alleviate psoriasis development^{48,49}, but the key role of PKR in psoriatic mice has not been specified previously.

Ds-cRNA knock-in dampens PKR-mediated inflammation in mice

Next, we asked whether ds-cRNA could dampen the activation of fast-responding inflammatory factors involved in IMQ-induced psoriatic mice. We generated ds-cRNA-constitutive overexpression mice using CRISPR-Cas9 with a fragment insertion at the *ROSA26* locus. The inserted fragment was driven by an EF1 α or a CAG promoter, followed by circularizable exons of the human circPOLR2A (9,10) containing the intramolecular dsRNA duplexes^{51,52} with flanking intronic complementary sequences (hereafter C_OE mice, Extended Data Fig. 7a). These designs allowed human circPOLR2A (9,10) to be produced using both promoters with a clear background in mice (Extended Data Fig. 7b,c).

Northern blot (NB) confirmed that the EF1 α -driven circPOLR2A (9,10) expressed at the highest level in spleen among examined tissues, while the CAG promoter mice showed a high circPOLR2A (9,10) expression in heart, lung and liver (Extended Data Fig. 7b). No discernible weight or other detectable difference was observed between the WT and littermates carrying the EF1 α promoter C_OE (Extended Data Fig. 7d), or between the WT and the CAG promoter C_OE mice (data not shown). These observations indicate that the supplementation of ds-cRNAs in vivo is unlikely to have affected the development of the mice even under constitutive expression and suggest that the use of ds-cRNAs as a therapeutic aptamer is likely to have minimal side effects.

We chose EF1 α promoter C_OE mice for subsequent analyses in spleens. About 400 copies of ds-cRNA per splenocyte were observed, which was estimated to come from a knocked-in C_OE mouse stem cell R1 line (Extended Data Fig. 7e,f). We first compared psoriatic phenotypes in WT and littermate C_OE mice on D1 and D2 IMQ. We observed a reduced expression of fast-responding inflammatory factors, including *Il6*, *Ifi44*, *Isg5* and *Mx2*, in psoriatic spleen cells of C_OE mice, compared to those in WT mice (Extended Data Fig. 8a). The same attenuated fast-responding inflammatory factors were also observed in B cells, T cells and monocytes (Fig. 3g,h), along with reduced p-PKR and its downstream p-eIF2 α in C_OE mice on D2 (Fig. 3i and Extended Data Fig. 8b). Consistently, C_OE mice exhibited a mild reduction in epidermal thickness (data not shown) compared to *Pkr*^{-/-} mice (Fig. 3f).

Fig. 3 | PKR knockout or genetic supplement of ds-cRNA alleviates inflammation in IMQ-induced psoriasis mice. a, Schematic of the IMQ-induced psoriasis inflammation mice model. **b**, The transient PKR/eIF2 α expression and prolonged PKR phosphorylation in IMQ animals. Left, western blot of PKR/eIF2 α expression and phosphorylation in spleens derived from IMQ mice ($n = 3$ at the indicated time point). Right, quantification with ImageJ and normalized to mActin; each dot represents one repeat. **c**, The expression of 721 high-confidence circRNAs of samples on D0, D1, D2 and D5. The CIRCscore⁴² of high-confidence circRNAs on D0 is significantly higher than those at subsequent time points. The fragments per billion mapped bases (FPB) value of each time point is the mean from the two repeats; each repeat includes two biologically independent animals. Data are shown as median and interquartile range. Wilcoxon rank-sum test, *** $P < 0.001$. **d**, DEGs are separated into six clusters according to their time-course expression patterns from D0 to D5. **e**, The expression level of fast-responding inflammatory factors in *Pkr*^{-/-} (gray line) and

paired WT (red line) mice spleens on consecutive IMQ treatments. Expression of each gene is shown by scaled fragments per kilobase of transcript per million mapped reads calculated by Mfuzz⁴⁴. **f**, *Pkr*^{-/-} mice showed mitigated epidermal thickness on IMQ treatment. Quantification of epidermal thickness from IMQ-D2 (WT, $n = 5$; *Pkr*^{-/-}, $n = 4$) was shown. **g**, Workflow of experiments shown in **h**. **h**, Human circPOLR2A (9, 10) dampens the inflammatory responses in splenocytes in IMQ mice. Relative expression of representative factors of the IFN α signaling pathway in C_OE mice ($n = 4$), compared to WT mice ($n = 5$) in B cells, T cells and monocytes of splenocytes on D1, determined by RT-qPCR. **i**, Human circPOLR2A (9, 10) dampens PKR activation in IMQ mice. PKR activation kinetics were analyzed in C_OE ($n = 5$) and WT ($n = 5$) mice on D2. The relative levels of p-PKR and p-eIF2 α in each tested mouse were quantified. **f, h, i**, Each dot represents one individual animal. NS, $P > 0.05$, * $P < 0.05$, ** $P < 0.01$, *** $P < 0.001$, two-tailed Student's *t*-test, data are shown as mean \pm s.d.

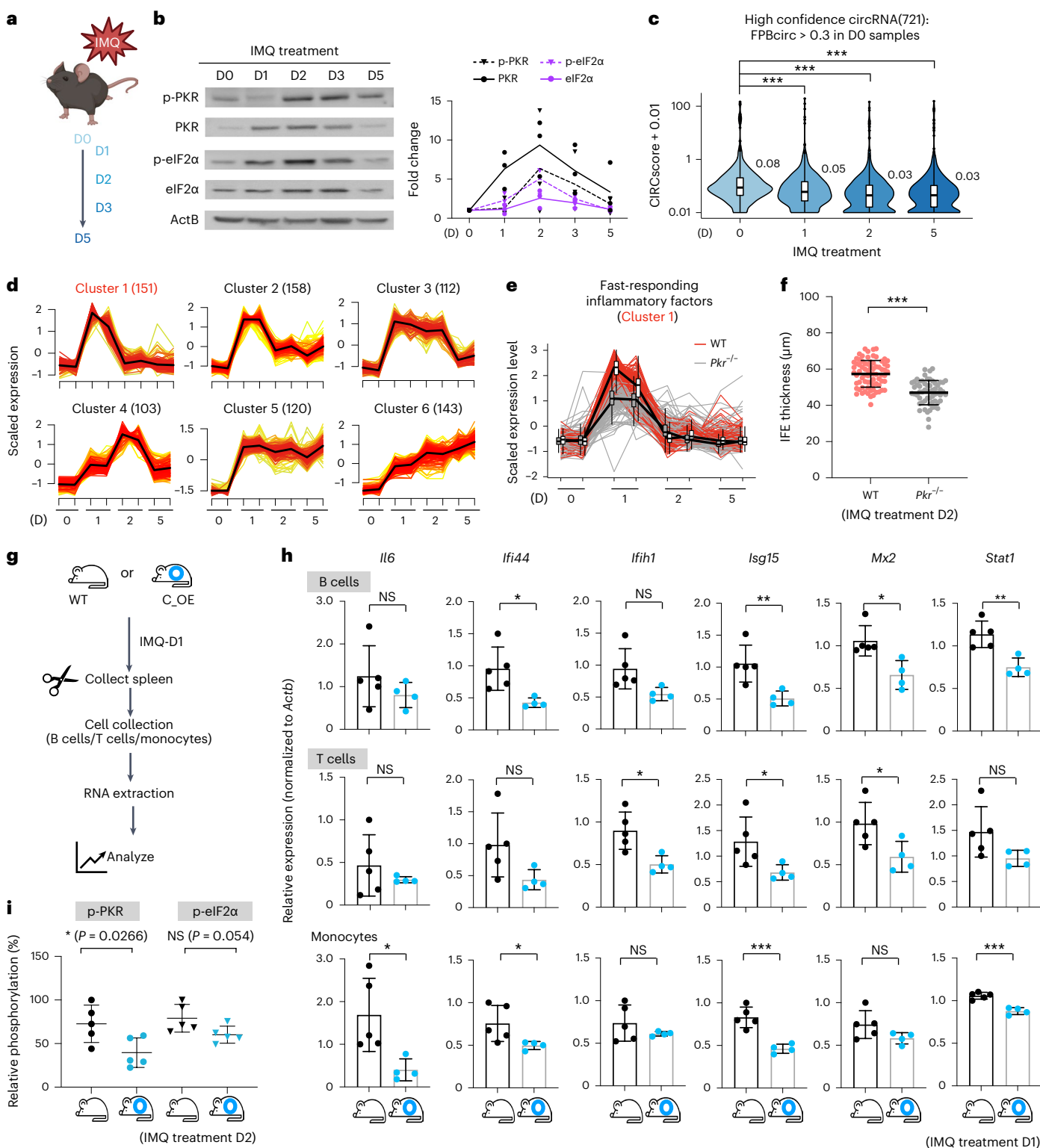
Such incomplete rescues at PKR cascade or epidermal thickness were due to activated RNase L at D1 IMQ (Extended Data Figs. 4c and 8c) leading to reduced circPOLR2A (9,10) in C_{OE} mice (Extended Data Fig. 8d).

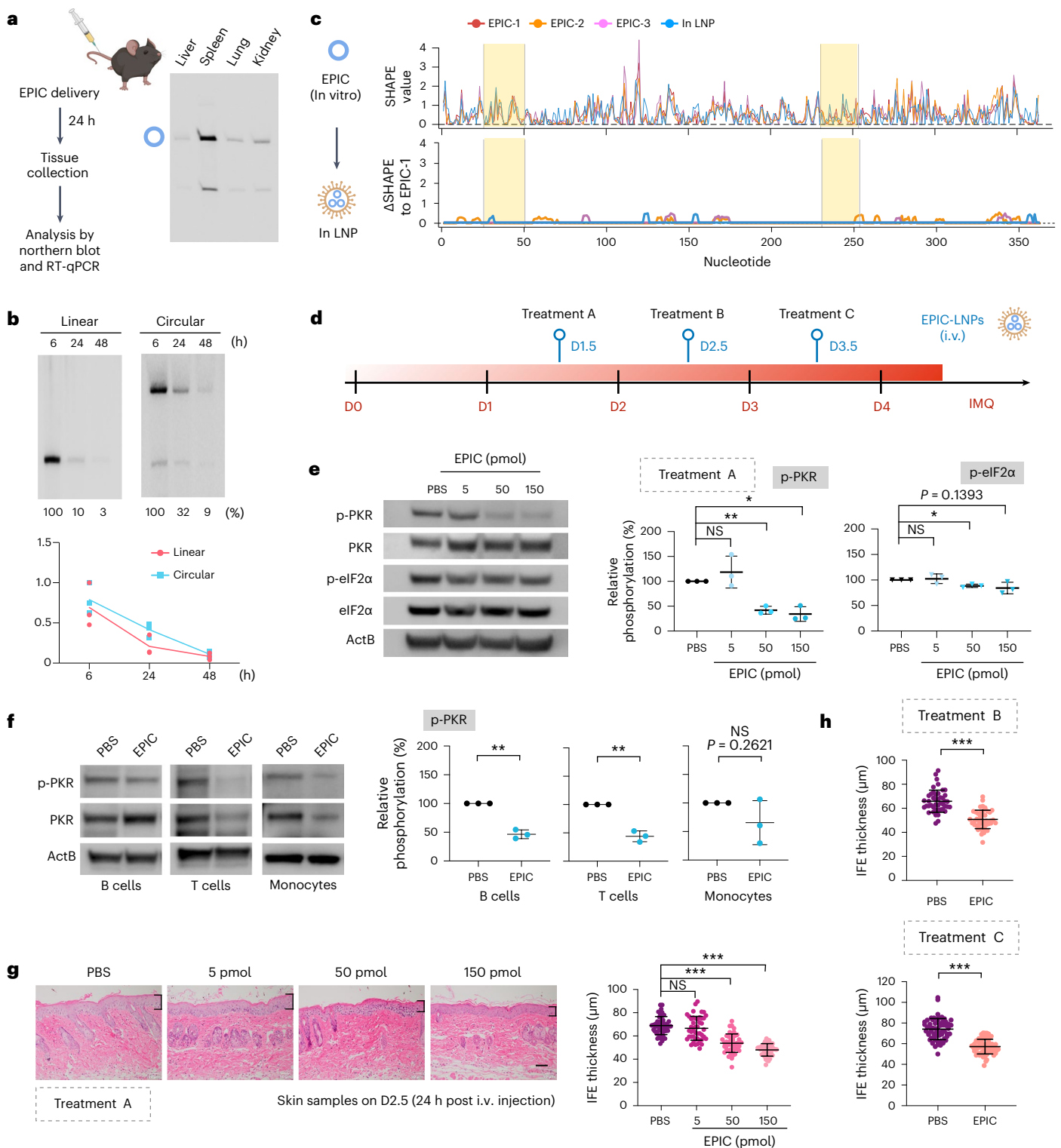
Delivery of EPICs in spleen is beneficial for psoriatic mice

To explore the therapeutic potential of synthesized ds-cRNAs, we attempted to deliver LNPs-encapsulated EPIC (EPIC-LNPs) to spleens with a reported formulation⁵³ (Extended Data Fig. 9a). Physicochemical characterization of EPIC-LNPs resulted in an average size of 86 ± 13.5 nm, polydispersity index of 0.059 ± 0.063 and zeta potential of -1.32 ± 0.54

(Extended Data Fig. 9b). Encapsulation efficiency was evaluated as 95.07% for EPIC-LNPs (Extended Data Fig. 9b). The consistent range of particle sizes of EPIC-LNPs was confirmed by a polydispersity index less than 0.1 (Extended Data Fig. 9b) and by transmission electron micrographs (Extended Data Fig. 9c).

We compared the turnover between ds-cRNAs and the linear cognates by intravenous (i.v.) injection of 1 μ g of LNP-encapsulated individual RNAs for spleen delivery (Fig. 4a), followed by NB at 6, 24 and 48 hours postinjection (Fig. 4b). These analyses showed at least a threefold lower turnover of EPICs than linear cognates in spleens





24 hours after i.v. injection, followed by an additional decay to less than 10% of their original level 48 hours after i.v. injection (Fig. 4b), revealing a prolonged turnover of ds-cRNAs compared to their linear cognates, albeit the linear cognates cannot fold into the desired conformation⁶.

We asked whether LNP encapsulation would alter EPIC folding status. Freshly made EPICs and EPIC-LNPs were subjected to circSHAPE-MaP, which showed comparable SHAPE signals (Fig. 4c). Further ΔSHAPE analysis showed that the slight difference in SHAPE reactivity resulting from LNP encapsulation was not higher than the variation of SHAPE reactivity among three biological replicates of

naked EPICs, indicating that the encapsulation procedure alone is unlikely to have altered EPIC conformation (Fig. 4c).

To ask whether EPIC-LNPs attenuate psoriatic phenotypes, we first injected 5, 50 and 150 pmol intravenously on D1.5 (Fig. 4d), after the D1 RNase L activation (Extended Data Fig. 4c). Psoriatic mice administered with EPIC-LNPs showed reduced p-PKR and p-eIF2α in spleens in a dose-dependent manner 24 hours after i.v. injection, while the expression of PKR and eIF2α remained largely unaltered (Fig. 4e). Further delineating the inhibitory effects of EPICs on PKR in splenocytes, including B cells, T cells and monocytes, all showed about 50% p-PKR

Fig. 4 | Spleen-targeted EPIC alleviates psoriasis phenotypes via dampening PKR activation. **a**, Optimized LNP enables the spleen-targeted RNA delivery. Left, workflow to resolve EPIC delivery profile. Right, an efficient spleen delivery of EPIC revealed by northern blot. **b**, EPIC shows a prolonged stability compared to linear POLR2A *in vivo*. Top, representative northern blot of EPIC and its linear isoform in spleens. Bottom, RT-qPCR analysis of three biologically independent animals, data are shown as dots and the means connected with lines. **c**, LNP encapsulation is unlikely to alter EPIC conformation. Left, schematic showing the conformational comparison of the naked EPIC of three repeats and in LNP by circSHAPE-MaP. Right top, SHAPE reactivity of each group was quantified at the single nucleotide resolution; right bottom, the profile of Δ SHAPE in absolute values between naked or LNP-encapsulated EPIC, compared to one of the naked EPIC samples. Yellow shadows mark the nucleotides of 23 bp imperfect dsRNA region. **d**, Schematic of ds-cRNA treatments for IMQ-induced psoriatic mice. **e**, Spleen-targeted delivery of EPIC reduces p-PKR *in vivo*. Left, the representative western blot of p-PKR and its downstream p-eIF2 α after EPIC delivery at different

EPIC concentrations. Right, quantification of p-PKR and p-eIF2 α from three independent experiments. **f**, Spleen-targeted delivery of EPIC attenuates p-PKR in different splenocytes. Psoriatic mice received Treatment A. B cells, T cells and monocytes were isolated and subjected to western blot. Left, the representative immunoblot of p-PKR after Treatment A in **d**. Right, quantification of p-PKR from three independent groups. Of note, each dot contains two littermates. **g**, Spleen-targeted delivery of EPIC reduces epidermal thickness in IMQ psoriatic mice on D1.5 EPIC-LNPs *i.v.* injection (Treatment A). Representative histological images of the dorsal skin sections from mice, stained by hematoxylin and eosin and quantified ($n = 3$ in each group). Black brackets mark the epidermis. Scale bars, 50 μ m. **h**, Spleen delivery of EPIC reduces epidermal thickness in IMQ psoriatic mice on D2.5 and D3.5 EPIC-LNPs *i.v.* injection (Treatments B and C in **d**), respectively. Epidermal thickness was quantified from mice treated with different treatments (D2.5, $n = 3$ in each group; D3.5, $n = 4$ in each group). **e–h**, NS, $P > 0.05$, $*P < 0.05$, $**P < 0.01$, $***P < 0.001$, two-tailed Welch's *t*-test for **e** and **g**, two-tailed Student's *t*-test for **f** and **h**, data are shown as mean \pm s.d.

reduction (Fig. 4f). These results indicated a general suppression of EPICs on PKR in independent cell types *in vivo*.

Consistently, the epidermal thickness was reduced to the level of that in *Pkr*^{-/-} mice, when administrated with the EPIC dosage at 50 pmol (Fig. 4g), at which p-PKR in psoriatic spleens was effectively inhibited (Fig. 4e). Total endogenous circRNAs 24 hours after EPIC-LNPs (*i.v.* injection) on D1.5 remained the same level as those without EPIC delivery (Extended Data Fig. 9d), indicating that such treatment did not affect endogenous circRNAs.

Furthermore, administrating EPIC-LNPs on D2.5 or D3.5 (Fig. 4h) displayed similarly roughly 25% reduced epidermis thickness to the D1.5 treatment (Fig. 4g). These results together indicated that synthesized ds-cRNAs dampened psoriatic regression via attenuating PKR-mediated inflammatory responses.

EPIC attenuates PKR-mediated inflammation in patient samples

Analyzing published datasets of lesional and nonlesional skins derived from patients with psoriasis^{19,20} revealed a similar reduction of overall circRNAs without much change in cognate mRNAs in lesional skins (Extended Data Fig. 10a), similar to observations in the psoriatic mice (Fig. 3c and Extended Data Fig. 4e). Consistent with previous reports⁵⁴, the IL-23–IL-17 axis and psoriasis-associated genes were augmented in lesional skins compared to nonlesional skins derived from patients (Extended Data Fig. 10b). We observed the same trend of elevated expression of fast-responding inflammatory factors, including PKR (*EIF2AK2*) in patients with psoriasis (Extended Data Fig. 10b). Finally, EPIC-LNPs rescued aberrant expression of psoriasis signature genes in PBMCs isolated from patients, diagnosed with the Psoriasis Area Severity Index^{55,56} (Supplementary Table 6). Such treatment resulted in reduced expression of transcripts for fast-responding inflammatory factors, such as IFI44 and IL6, as well as psoriasis signature factors IL17A, IL23A and IL23R (Extended Data Fig. 10c).

Discussion

The unique circRNAs' conformation^{5,6}, stability^{3,4} and immunogenicity^{7,8,57} have endowed them with potential for therapeutic advantages. Evidence of engineered translatable circRNAs shows potential in vaccine development⁵⁸ and protein therapies²⁵. Our results indicate RNA circles as potential therapeutic aptamers in dampening psoriatic progression through targeting PKR (Figs. 2–4).

We have optimized the PIE system for simple and scalable synthesis of RNA circles with minimized immunogenicity (Fig. 1 and Extended Data Fig. 1), including aptamers suppressing PKR (Fig. 1e), and those for translation up to around 7,000 nt (Fig. 1d and Extended Data Fig. 1a), broadening the capacity of designing circRNA-based modalities. Synthesized ds-cRNA displayed a remarkable stability for PKR association (Fig. 2 and Extended Data Figs. 2 and 3), highlighting that the circular

conformation ensures its tertiary folding to confine PKR movement, thereby effectively suppressing p-PKR. Future determination of atomic structures of ds-cRNA-PKR complexes will be of interest for understanding the molecular basis.

Suppression of PKR activity could attenuate auto-inflammatory responses in cells derived from patients with SLE⁶, patients with psoriasis (Extended Data Fig. 10) and in psoriatic mice (Figs. 3 and 4), all of which exhibited disease pathology at least partially driven by unwanted PKR activation. However, no PKR inhibitor has been approved in clinic due to off-target effects, cell toxicity and inability to manipulate PKR in specific cell types *in vivo*^{16,17,59,60}. In another example, neuroinflammation has been increasingly recognized as a major driver of brain disorders, including Alzheimer's disease⁶¹. *Pkr*^{-/-} mice showed alleviated Alzheimer's disease neuroinflammation and improved learning capability^{62,63}, and a similar ds-cRNA therapy could rescue neurogenerative phenotypes in Alzheimer's disease models by dampening PKR activity⁶⁴.

Targeting pathological PKR activity could be immunosuppressive, similar to the anti-IL-17 therapy for psoriasis^{65,66}. This may pose challenge in patients with chronic virus infections, even though the anti-IL-17 therapy appears safe in patients with chronic infections when combined with antiviral prophylaxis^{65,66}. In addition, while no toxicity was observed in mice carrying ds-cRNAs for at least 12 months (Extended Data Fig. 7d), the additional long-term safety and tolerability of ds-cRNAs await further investigation. Finally, despite the targeted spleen delivery of ds-cRNAs (Fig. 4), the fact that ds-cRNAs-mediated PKR suppression is cell-type independent (Fig. 4f) prompts future development of topical EPIC delivery to alleviate local inflammation.

Online content

Any methods, additional references, Nature Portfolio reporting summaries, source data, extended data, supplementary information, acknowledgements, peer review information; details of author contributions and competing interests; and statements of data and code availability are available at <https://doi.org/10.1038/s41587-024-02204-4>.

References

- Hause, A. M. et al. Safety monitoring of bivalent COVID-19 mRNA vaccine booster doses among persons aged ≥ 12 years—United States, August 31–October 23, 2022. *MMWR Morb. Mortal Wkly Rep.* **71**, 1401–1406 (2022).
- Winkle, M., El-Daly, S. M., Fabbri, M. & Calin, G. A. Noncoding RNA therapeutics—challenges and potential solutions. *Nat. Rev. Drug Discov.* **20**, 629–651 (2021).
- Enuka, Y. et al. Circular RNAs are long-lived and display only minimal early alterations in response to a growth factor. *Nucleic Acids Res.* **44**, 1370–1383 (2016).

4. Zhang, Y. et al. The biogenesis of nascent circular RNAs. *Cell Rep.* **15**, 611–624 (2016).
5. Fischer, J. W., Busa, V. F., Shao, Y. & Leung, A. K. L. Structure-mediated RNA decay by UPF1 and G3BP1. *Mol. Cell.* **78**, 70–84.e76 (2020).
6. Liu, C. X. et al. Structure and degradation of circular RNAs regulate PKR activation in innate immunity. *Cell* **177**, 865–880.e821 (2019).
7. Wesselhoeft, R. A. et al. RNA circularization diminishes immunogenicity and can extend translation duration in vivo. *Mol. Cell.* **74**, 508–520.e504 (2019).
8. Liu, C. X. et al. RNA circles with minimized immunogenicity as potent PKR inhibitors. *Mol. Cell.* **82**, 420–434.e426 (2022).
9. Liu, C. X. & Chen, L. L. Circular RNAs: characterization, cellular roles, and applications. *Cell* **185**, 2390 (2022).
10. Bou-Nader, C., Gordon, J. M., Henderson, F. E. & Zhang, J. The search for a PKR code-differential regulation of protein kinase R activity by diverse RNA and protein regulators. *RNA* **25**, 539–556 (2019).
11. Cao, S. S., Song, B. & Kaufman, R. J. PKR protects colonic epithelium against colitis through the unfolded protein response and prosurvival signaling. *Inflamm. Bowel Dis.* **18**, 1735–1742 (2012).
12. Grolleau, A., Kaplan, M. J., Hanash, S. M., Beretta, L. & Richardson, B. Impaired translational response and increased protein kinase PKR expression in T cells from lupus patients. *J. Clin. Invest.* **106**, 1561–1568 (2000).
13. Rath, E. et al. Induction of dsRNA-activated protein kinase links mitochondrial unfolded protein response to the pathogenesis of intestinal inflammation. *Gut* **61**, 1269–1278 (2012).
14. Zheng, X. & Bevilacqua, P. C. Activation of the protein kinase PKR by short double-stranded RNAs with single-stranded tails. *RNA* **10**, 1934–1945 (2004).
15. Ingrand, S. et al. The oxindole/imidazole derivative C16 reduces in vivo brain PKR activation. *FEBS Lett.* **581**, 4473–4478 (2007).
16. Mouton-Liger, F. et al. PKR downregulation prevents neurodegeneration and β -amyloid production in a thiamine-deficient model. *Cell Death Dis.* **6**, e1594 (2015).
17. Watanabe, T. et al. Therapeutic effects of the PKR inhibitor C16 suppressing tumor proliferation and angiogenesis in hepatocellular carcinoma in vitro and in vivo. *Sci. Rep.* **10**, 5133 (2020).
18. Griffiths, C. E. M., Armstrong, A. W., Gudjonsson, J. E., & Barker, J. Psoriasis. *Lancet* **397**, 1301–1315 (2021).
19. Moldovan, L. I. et al. High-throughput RNA sequencing from paired lesional- and non-lesional skin reveals major alterations in the psoriasis circRNAome. *BMC Med. Genomics* **12**, 174 (2019).
20. Moldovan, L. I. et al. Characterization of circular RNA transcriptomes in psoriasis and atopic dermatitis reveals disease-specific expression profiles. *Exp. Dermatol.* **30**, 1187–1196 (2021).
21. Seeler, S. et al. Global circRNA expression changes predate clinical and histological improvements of psoriasis patients upon secukinumab treatment. *PLoS ONE* **17**, e0275219 (2022).
22. Swindell, W. R. et al. Imiquimod has strain-dependent effects in mice and does not uniquely model human psoriasis. *Genome Med.* **9**, 24 (2017).
23. Obi, P. & Chen, Y. G. The design and synthesis of circular RNAs. *Methods* **196**, 85–103 (2021).
24. Puttaraju, M. & Been, M. D. Group I permuted intron-exon (PIE) sequences self-splice to produce circular exons. *Nucleic Acids Res.* **20**, 5357–5364 (1992).
25. Wesselhoeft, R. A., Kowalski, P. S. & Anderson, D. G. Engineering circular RNA for potent and stable translation in eukaryotic cells. *Nat. Commun.* **9**, 2629 (2018).
26. Guo, S. K., Nan, F., Liu, C. X., Yang, L. & Chen, L. L. Mapping circular RNA structures in living cells by SHAPE-MaP. *Methods* **196**, 47–55 (2021).
27. Kuhen, K. L. et al. Structural organization of the human gene (PKR) encoding an interferon-inducible RNA-dependent protein kinase (PKR) and differences from its mouse homolog. *Genomics* **36**, 197–201 (1996).
28. Samuel, C. E. The eIF-2 alpha protein kinases, regulators of translation in eukaryotes from yeasts to humans. *J. Biol. Chem.* **268**, 7603–7606 (1993).
29. Wu, M. et al. lncRNA SLERT controls phase separation of FC/DFCs to facilitate Pol I transcription. *Science* **373**, 547–555 (2021).
30. Yang, X. W. et al. MutS functions as a clamp loader by positioning MutL on the DNA during mismatch repair. *Nat. Commun.* **13**, 5808 (2022).
31. Hummert, J. et al. Photobleaching step analysis for robust determination of protein complex stoichiometries. *Mol. Biol. Cell.* **32**, ar35 (2021).
32. Yuan, J., He, K., Cheng, M., Yu, J. & Fang, X. Analysis of the steps in single-molecule photobleaching traces by using the hidden Markov model and maximum-likelihood clustering. *Chem. Asian J.* **9**, 2303–2308 (2014).
33. Nallagatla, S. R., Toroney, R. & Bevilacqua, P. C. Regulation of innate immunity through RNA structure and the protein kinase PKR. *Curr. Opin. Struct. Biol.* **21**, 119–127 (2011).
34. Heinicke, L. A., Nallagatla, S. R., Hull, C. M. & Bevilacqua, P. C. RNA helical imperfections regulate activation of the protein kinase PKR: effects of bulge position, size, and geometry. *RNA* **17**, 957–966 (2011).
35. Yan, Y., Tao, H., He, J. & Huang, S. Y. The HDock server for integrated protein-protein docking. *Nat. Protoc.* **15**, 1829–1852 (2020).
36. Husain, B., Hesler, S. & Cole, J. L. Regulation of PKR by RNA: formation of active and inactive dimers. *Biochemistry* **54**, 6663–6672 (2015).
37. Mayo, C. B. et al. Structural basis of protein kinase R autophosphorylation. *Biochemistry* **58**, 2967–2977 (2019).
38. Dörner, T. & Furie, R. Novel paradigms in systemic lupus erythematosus. *Lancet* **393**, 2344–2358 (2019).
39. Tsokos, G. C., Lo, M. S., Costa Reis, P. & Sullivan, K. E. New insights into the immunopathogenesis of systemic lupus erythematosus. *Nat. Rev. Rheumatol.* **12**, 716–730 (2016).
40. van der Fits, L. et al. Imiquimod-induced psoriasis-like skin inflammation in mice is mediated via the IL-23/IL-17 axis. *J. Immunol.* **182**, 5836–5845 (2009).
41. Taylor, S. S., Haste, N. M. & Ghosh, G. PKR and eIF2alpha: integration of kinase dimerization, activation, and substrate docking. *Cell* **122**, 823–825 (2005).
42. Ma, X. K. et al. CIRCexplorer3: a CLEAR pipeline for direct comparison of circular and linear RNA expression. *Genom. Proteom. Bioinform.* **17**, 511–521 (2019).
43. Futschik, M. E. & Carlisle, B. Noise-robust soft clustering of gene expression time-course data. *J. Bioinform. Comput. Biol.* **3**, 965–988 (2005).
44. Kumar, L. & M, E. F. Mfuzz: a software package for soft clustering of microarray data. *Bioinformatics* **2**, 5–7 (2007).
45. Lande, R. & Gilliet, M. Plasmacytoid dendritic cells: key players in the initiation and regulation of immune responses. *Ann. N. Y. Acad. Sci.* **1183**, 89–103 (2010).
46. Chiricozzi, A., Romanelli, P., Volpe, E., Borsellino, G. & Romanelli, M. Scanning the immunopathogenesis of psoriasis. *Int. J. Mol. Sci.* **19**, 179 (2018).
47. Yang, Y. L. et al. Deficient signaling in mice devoid of double-stranded RNA-dependent protein kinase. *EMBO J.* **14**, 6095–6106 (1995).

48. Nestle, F. O. et al. Plasmacytoid predendritic cells initiate psoriasis through interferon-alpha production. *J. Exp. Med.* **202**, 135–143 (2005).
49. Rácz, E. et al. Narrowband ultraviolet B inhibits innate cytosolic double-stranded RNA receptors in psoriatic skin and keratinocytes. *Br. J. Dermatol.* **164**, 838–847 (2011).
50. Zhang, L. J. et al. Antimicrobial peptide LL37 and MAVS signaling drive interferon- β production by epidermal keratinocytes during skin injury. *Immunity* **45**, 119–130 (2016).
51. Chen, L. L. et al. A guide to naming eukaryotic circular RNAs. *Nat. Cell Biol.* **25**, 1–5 (2023).
52. Zhang, X. O. et al. Complementary sequence-mediated exon circularization. *Cell* **159**, 134–147 (2014).
53. Naidu, G. S. et al. A combinatorial library of lipid nanoparticles for cell type-specific mRNA delivery. *Adv. Sci.* **10**, e2301929 (2023).
54. Jones, S. A. et al. GILZ regulates Th17 responses and restrains IL-17-mediated skin inflammation. *J. Autoimmun.* **61**, 73–80 (2015).
55. Fredriksson, T. & Pettersson, U. Severe psoriasis-oral therapy with a new retinoid. *Dermatologica* **157**, 238–244 (1978).
56. Langley, R. G. & Ellis, C. N. Evaluating psoriasis with psoriasis area and severity index, psoriasis global assessment, and lattice system physician's global assessment. *J. Am. Acad. Dermatol.* **51**, 563–569 (2004).
57. Chen, Y. G. et al. N6-methyladenosine modification controls circular RNA immunity. *Mol. Cell.* **76**, 96–109.e109 (2019).
58. Qu, L. et al. Circular RNA vaccines against SARS-CoV-2 and emerging variants. *Cell* **185**, 1728–1744.e1716 (2022).
59. Gal-Ben-Ari, S., Barrera, I., Ehrlich, M. & Rosenblum, K. PKR: a kinase to remember. *Front. Mol. Neurosci.* **11**, 480 (2018).
60. Tronel, C., Page, G., Bodard, S., Chalon, S. & Antier, D. The specific PKR inhibitor C16 prevents apoptosis and IL-1 β production in an acute excitotoxic rat model with a neuroinflammatory component. *Neurochem. Int.* **64**, 73–83 (2014).
61. Chang, R. C. et al. Involvement of double-stranded RNA-dependent protein kinase and phosphorylation of eukaryotic initiation factor-2 α in neuronal degeneration. *J. Neurochem.* **83**, 1215–1225 (2002).
62. Stern, E., Chinnakkaruppan, A., David, O., Sonenberg, N. & Rosenblum, K. Blocking the eIF2 α kinase (PKR) enhances positive and negative forms of cortex-dependent taste memory. *J. Neurosci.* **33**, 2517–2525 (2013).
63. Zhu, P. J. et al. Suppression of PKR promotes network excitability and enhanced cognition by interferon-gamma-mediated disinhibition. *Cell* **147**, 1384–1396 (2011).
64. Feng, X. et al. Circular RNA aptamers ameliorate AD-relevant phenotypes by targeting PKR. Preprint at *bioRxiv* <https://doi.org/10.1101/2024.03.27.583257> (2024).
65. Kaushik, S. B. & Lebwohl, M. G. Psoriasis: which therapy for which patient: psoriasis comorbidities and preferred systemic agents. *J. Am. Acad. Dermatol.* **80**, 27–40 (2019).
66. Manfreda, V., Esposito, M., Campione, E., Bianchi, L. & Giunta, A. Apremilast efficacy and safety in a psoriatic arthritis patient affected by HIV and HBV virus infections. *Postgrad. Med.* **131**, 239–240 (2019).

Publisher's note Springer Nature remains neutral with regard to jurisdictional claims in published maps and institutional affiliations.

Springer Nature or its licensor (e.g. a society or other partner) holds exclusive rights to this article under a publishing agreement with the author(s) or other rightsholder(s); author self-archiving of the accepted manuscript version of this article is solely governed by the terms of such publishing agreement and applicable law.

© The Author(s), under exclusive licence to Springer Nature America, Inc. 2024

Methods

Plasmid construction

Different versions of *Anabaena* PIE carrying the sequence of interest were constructed to the downstream of a T7 promoter in a pUC57-based backbone plasmid as the IVT template. To synthesize circPOLR2A (9, 10) with different junction sites, the full length of circPOLR2A (9, 10) was amplified by PCR with reverse transcription (RT-PCR) with different primer pairs and constructed into Ana_PIE_27nt plasmids. All constructs were confirmed by Sanger sequencing. All related sequences are listed in Supplementary Table 7.

To construct protein purification plasmids, the PKR coding sequence were constructed into pET-28a vector, Hexa-histidine (6xHis) and sortase recognition sequence (srt, LPETG) were tagged on the C terminus of the PKR coding sequence for sortase-mediated peptide ligation⁶⁷. The PKR-ΔIDR truncation was constructed similarly.

Cell culture, transfection and stimulation

The human cell line, A549 cell line (SCSP-503), was provided by the Cell Bank, Chinese Academy of Sciences (CAS), and was cultured in F-12K supplemented with 10% fetal bovine serum and 1% GlutaMax. The same amount of RNAs synthesized in vitro and poly(I:C) (200 ng for each sample) were transfected using Lipofectamine MessengerMax reagent (Thermo) in A549 cells according to the manufacturer's protocols. About 70–80% transfection efficiency was achieved in A549 cells. Total RNAs were collected after 6 h transfection for analyses.

RNA isolation, RT-PCR, RT-qPCR and northern blot

Total RNAs from cultured cells, or different tissues of mice, were extracted with TRIzol (Life technologies) according to the manufacturer's protocol. Complementary DNAs (cDNAs) were reverse transcribed with SuperScript III (Invitrogen) or PrimeScript RT Master Mix (Takara) and applied for PCR or quantitative PCR (qPCR) analysis. 18S rRNA, mActin were examined as internal controls. Expression of each examined gene was determined from three independent experiments. For the detection of RNase L activation, RtcB ligase-assisted qPCR were performed as described with a slight modification^{6,68}. Briefly, total RNAs were purified and RNAs with 2'-3' cyclic phosphate were ligated to the adapter 5'-rGrArUrCrGrUCGGACTGTAGAACTCTGAAC-3' using RtcB ligase. The resulting cDNAs were assessed for RNase L cleavage products by qPCR and normalized to U6.

Northern blot was performed according to the manufacturer's protocol (DIG Northern Starter Kit, Roche). In brief, 5 µg total RNA was resolved on denaturing PAGE, transferred to nylon membrane (Roche) and ultraviolet crosslinked. Membrane was then hybridized with Digoxigenin-labeled antisense riboprobes. Primers and northern blot probe are listed in Supplementary Table 7.

In vitro RNA transcription, circularization and purification

Template vectors were linearized with HindIII-HF (NEB) and cleaned up. RNAs were in vitro transcribed from 1 µg linearized templates in a 20 µl reaction with the RiboMax system (Promega). To produce RNA circles or hairpin RNA labeled with biotin and Cy5, Biotin-16-UTP (0.25 mM) and Cy5-UTP (0.25 mM) were incorporated into the IVT reaction. For circularization with T4 RNA ligase I (NEB), precursors were transcribed with a 5:1 molar ratio of GMP to GTP in reactions and then subjected to ligation as described⁸. For circularization with all versions of *Anabaena* PIE, precursors were transcribed in vitro following the manufacturer's protocol and column purified with MEGAclear kit (Invitrogen). 50 µg of PIE transcription products were heated to 70 °C for 3 min and immediately placed on ice for 2 min, then 2 mM of GTP and T4 RNA ligase buffer (NEB) were added for 8 min of incubation at 55 °C. Products of T4 ligation or PIE self-splicing were column purified, respectively.

For the optimized RNase R digestion⁶⁹, 50 µg of products above were subjected to A-tailing reaction with *Escherichia coli* Poly(A)

polymerase (Tinzyme) following the manufacturer's instructions. After A-tailing, the RNAs were incubated at 37 °C for 1 h with 15 U of RNase R (Tinzyme) and heated at 75 °C for 5 min. Afterward, the RNAs were treated with 10 U of FastAP (Thermo Scientific) at 37 °C for 30 min, stopped by heating at 75 °C for 5 min and column purified. Synthesized RNAs mentioned above were quantified using a NanoDrop One spectrophotometer (Thermo Scientific) and analyzed with denaturing PAGE using 8 M urea gels in Tris-Borate-EDTA (TBE) running buffer.

The linear 79, 33 and 23 bp dsRNAs were synthesized with biotin or Cy5 terminally labeled at two separated strands, respectively (Supplementary Table 7). The RNA circle of 27 nt (Extended Data Fig. 1f) was circularized from a synthesized 5'-monophosphate RNA oligo (Sangon), using T4 RNA ligase I (NEB), and purified with PAGE.

Protein expression, purification and labeling

PKR proteins were purified as described in the previous report⁸. Expression plasmids or His-tagged proteins (PKR) were transformed into *E. coli* Rosetta 2 (DE3) competent cells (Sigma). Then 5 ml of Luria-Bertani (LB) culture supplemented with 100 µg l⁻¹ kanamycin was incubated overnight (220 rpm, 37 °C) with a single colony, then the culture was diluted 100-fold into 1 l of LB culture supplemented with 100 µg l⁻¹ kanamycin. On optical density at 600 nm reaching 0.4, protein expression was induced with 0.8 mM isopropyl-β-D-thiogalactoside overnight (100 rpm, 16 °C). Cell pellets were collected by centrifugation (5,000g, 10 min, 4 °C), resuspended in lysis buffer (50 mM Tris-HCl pH 8.0, 500 mM NaCl, 20 mM imidazole, 10% glycerol, 1 mM phenylmethylsulfonyl fluoride (PMSF)) supplemented with 1 mg ml⁻¹ lysozyme and stored on ice for 30 min, followed by 5 min (800 bar, 60 strokes per min, 4 °C) disruption (UNION-BIOTECH, UH-06). After centrifugation (10,000g, 30 min, 4 °C), supernatants were incubated with Ni Sepharose (GE healthcare) for 2 h at 4 °C. The Sepharose was washed with washing buffer (50 mM Tris-HCl pH 8.0, 500 mM NaCl, 40 mM imidazole, 1 mM PMSF), and bound protein was eluted with elution buffer (50 mM Tris pH 8.0, 500 mM NaCl, 300 mM imidazole). Concentration of purified protein was measured by the Modified Bradford Protein Assay Kit (Sangon Biotech) and further resolved by SDS-PAGE.

For smTIRF analysis, LPETG-labeled PKR was pooled and dialyzed overnight in labeling buffer (50 mM Tris-HCl pH 8.0, 500 mM NaCl, 10 mM CaCl₂ and 10% glycerol). The protein fractions were then incubated with sortase and GGGC-Cy3 peptides (for C-terminal labeling, ChinaPeptides) at 4 °C for 1 h (protein:sortase:peptide, 1:2:5). Labeled PKR was diluted with double volume of buffer C (25 mM HEPES pH 7.8, 1 mM DTT, 10% glycerol and 0.1 mM EDTA) and loaded onto a heparin column, washed with buffer C plus 100 mM NaCl and eluted with buffer C plus 1 M NaCl. PKR-containing fractions were dialyzed in storage buffer (25 mM HEPES pH 7.8, 1 mM DTT, 0.1 mM EDTA, 500 mM NaCl and 20% glycerol) and stored at -80 °C. Concentrations and labeling efficiencies were determined by comparing protein absorbance at 280 nm with Cy3 absorbance at 550 nm and the labeling efficiency was about 50%.

In vitro activation assay of PKR

In vitro activation assay of PKR was performed as described¹⁴ with modifications. Briefly, equal amounts of the purified 79 nt RNA top strand (TS79R) and bottom strand (BS79R) were annealed in TEN₁₀₀ (10 mM Tris-HCl pH 7.5, 1 mM EDTA and 100 mM NaCl) for 1 min at 95 °C followed by cooling on the bench for 10 min. The ability of various RNAs to activate or inhibit PKR kinase was determined by PKR auto-phosphorylation assays. Purified PKR was first dephosphorylated by λ-PPase (NEB), as described in ref. 70. Subsequently, λ-PPase was inactivated by sodium orthovanadate⁷⁰. Next, 10 µCi [γ-³²P]ATP, 0.6 µM dephosphorylated PKR, and different RNAs were incubated in 20 mM HEPES (pH 7.5), 4 mM MgCl₂, 100 mM KCl and 1 mM ATP for 30 min at 30 °C. Reactions were stopped by adding SDS loading buffer

and resolved on 4–12% Bis-Tris PAGE. Autoradiography and immunoblotting were visualized, and quantified by ImageJ.

Generation of C_{OE} mice

The ds-cRNA constitutively overexpressed mice were generated on the C57BL/6 genetic background. Briefly, a fragment was inserted at the ROSA26 locus, which contains an EF1 α promoter or a CAG promoter, respectively, the future circularized exons of the human circPOLR2A (9, 10), and flanking introns with complementary sequences in an orientation-opposite pattern. Southern blotting and restriction enzyme digestion confirmed proper integration. The correctly targeted embryonic stem clones were injected into C57BL/6 blastocysts to generate C_{OE} mice. To genotype the mice, genomic fragments were amplified from tail DNAs using designed specific primers (Supplementary Table 7).

Generation of *Pkr*^{-/-} mice

Eif2ak2 (PKR) knockout mice (strain no. T015370) were purchased from GemPharmatech. Exon 3 of *Eif2ak2-201* (ENSMUST00000024884.4) transcript was recommended as the knockout region. A single 2,637 bp fragment containing a 121 bp coding sequence was deleted by the CRISPR–Cas9 system, resulting in disruption of protein function, as confirmed by western blot in Extended Data Fig. 6a.

Animal use and care

Mice were bred and maintained under the specific-pathogen-free condition at the Center for Excellence in Molecular Cell Science (CEMCS), CAS. Unless otherwise stated, male mice were used at 6–8 weeks of age. Of note, experiments conducted in male mice are representative of those in female mice of C57BL/6 background (data not shown). The mouse experiments were carried out in accordance with the institutional guidelines and were approved by the Institutional Animal Care and Use Committees at CEMCS, CAS.

Patients with psoriasis

All patients with psoriasis were recruited from Beijing Chao-Yang Hospital, Capital Medical University. All patients were diagnosed according to Psoriasis Area Severity Index score^{55,56} (Supplementary Table 6). The study was approved by the Research Ethics Board of Beijing Chao-Yang Hospital, Capital Medical University. Written informed consent was signed before the sample collection.

IMQ-induced psoriasis mouse model

WT, *Pkr*^{-/-} and C_{OE} mice received a daily topical dose of 62.5 mg IMQ cream (5%; Aldara; 3M Pharmaceuticals) on the shaved dorsal skin for 1–5 days. Control mice were conducted similarly without the IMQ treatment or with Vaseline treatment. Samples used for RNA and protein analyses were taken 24 h after the last treatment. Spleen samples were treated with Red cell lysis buffer (Tiangen) and washed with PBS. B cells, T cells and monocytes were isolated with corresponding EasySep Mouse Kit (Stemcell).

Histopathology

For histopathology analysis, mouse dorsal skin were fixed with 4% PFA overnight followed by dehydration and embedding in paraffin. Tissue sections of 0.5-mm thickness were stained with hematoxylin and eosin using standard procedures. Stained sections were scanned using an Olympus microscope (BX53).

Western blot

Cells were collected after treatments and resuspended in RIPA lysis buffer with protease and phosphatase inhibitor cocktail (Beyotime) for 10 min at 4 °C. After centrifugation, supernatants containing soluble proteins were resolved on 4–12% Bis-Tris polyacrylamide gels (GenScript) and analyzed by western blot with anti-PKR (Santa Cruz, 1:1,000

dilution), anti-phos-PKR (Sigma, 1:500 dilution), anti-EIF2 α (ABclonal, 1:500 dilution), anti-phos-EIF2 α (Abcam, 1:500 dilution) or anti-ACTB (Sigma, 1:5,000 dilution) antibodies.

LNP preparation and characterization

LNPs were prepared using a microfluidic mixing device as described previously⁵³. Briefly, RNA payloads were suspended in 25 mM acetate buffer (pH 4.5) and lipids were mixed in ethanol. To create LNPs, a dual-syringe pump was used to transport the two solutions through the NanoAssembler Ignite microfluidic mixer (Precision NanoSystems) at a total flow rate of 12 ml min⁻¹. The particles were then dialyzed overnight against PBS. Particles in PBS were analyzed for size and uniformity by dynamic light scattering. Zeta potential was determined using the Malvern Zetasizer. RNA encapsulation in LNPs was calculated with the Quant-iT RiboGreen RNA assay kit (Thermo Fisher Scientific) by calculating the percentage encapsulation at 100% – (RNA-LNPs/RNA-LNPs with Triton X-100).

SHAPE probing (with or without proteins) and SHAPE-MaP reverse transcription

In vitro SHAPE probing was performed as described^{6,26,71} with modifications. In vitro transcribed and purified human 5S rRNA/circRNAs were refolded in 3.3 \times folding buffer (333 mM HEPES, pH 8.0; 333 mM NaCl; 33 mM MgCl₂). After refolding, RNAs were incubated with 100 mM of NAI (EMD Millipore) in dimethylsulfoxide (DMSO) for 10 min at 37 °C. For each set of in vitro SHAPE probing with proteins, 1.5 pmol of RNAs were incubated with 12 pmol of purified and dephosphorylated PKR protein, followed by NAI modification at 100 mM or with DMSO for 10 min at 37 °C. For RNAs within LNP, ds-cRNAs were capsulated with LNP as described above and subjected to SHAPE probing without additional folding. A denaturing control reaction was performed in parallel: RNAs were suspended in a denaturing buffer containing formamide and incubated at 95 °C before modification with NAI. After probing, RNAs were extracted with phenol:chloroform:isoamyl alcohol (25:24:1), ethanol precipitated and dissolved in nuclease-free water.

About 50–200 ng of RNAs were obtained under each treatment and were then reverse transcribed with 200 U of SuperScript II (Invitrogen), 6 mM MnCl₂ and gene-specific primers for linear or circRNAs (5S rRNA was used as a spike-in control). cDNAs were purified with RNAClean XP (Beckman Coulter). Second-strand synthesis was performed with Q5 hot start high-fidelity DNA polymerase. The resulting PCR products were further isolated with StarPrep Gel Extraction Kit (GenStar). All related primers are listed in Supplementary Table 7.

SHAPE-MaP library preparation and sequencing

In vitro synthesized circRNAs at each condition were used as one sample to build a library. In brief, SHAPE-MaP libraries were prepared from 1 ng of DNAs reverse transcribed from circular SHAPE RNA, and size-selected with AmpureXP beads (Agencourt) with a 1:1 (bead to sample) ratio to obtain library DNA products spanning 100–400 bp in length. Final libraries were quantified using the Agilent Bioanalyzer 2100 and QuBit high-sensitivity double-stranded DNA assay. Deep sequencing was performed by the Illumina HiSeq X Ten platform at the CAS Key Laboratory of Computational Biology Omics Core, Shanghai, China. About 5–15 million sequencing reads were obtained for each sample, with 86% of bases at or above Q30.

smTIRF microscopy

All smTIRF data were acquired on a custom-built prism-type TIRF microscope established on an Olympus IX73. Fluorophores were excited using the 532- and 637-nm laser lines. Image acquisition was performed using an EMCCD camera (iXon Ultra 897, Andor) after splitting emissions by an optical setup (OptoSplit II emission image splitter, Cairn Research). Micro-Manager image capture software was used to control the laser excitation.

The Cy5–biotin labeled RNA (150 pM) in 300 μ l of T50 buffer (20 mM Tris-HCl pH 7.5, 50 mM NaCl, RNase inhibitor) was injected into a custom-made flow cell chamber by laminar flow (25 μ l min⁻¹). RNA was immobilized on a neutravidin-coated, PEG passivated quartz slide surface, and the unbound RNA was flushed by imaging buffer A (20 mM Tris-HCl pH 7.5, 0.1 mM DTT, 0.2 mg ml⁻¹ acetylated BSA (Molecular Cloning Laboratories), 0.0025% P-20 surfactant (GE healthcare), 5 mM MgCl₂, and 100 mM NaCl, RNase inhibitor). To minimize photoblinking and photobleaching, imaging buffer A was supplemented with a photostability enhancing and oxygen scavenging cocktail containing saturated Trolox (roughly 3 mM) and a PCA (protocatechuic acid)–PCD (protocatechuate-3,4-dioxygenase) oxygen scavenger system composed of PCA (1 mM) and PCD (10 nM)⁷².

To measure the PKR–RNA binding activity and lifetime, roughly 1–5 nM PKR–Cy3 in imaging buffer A was injected into the flow cell chamber by laminar flow (25 μ l min⁻¹) and the PKR–RNA interactions were monitored in real time (roughly 23 °C).

To determine the survival lifetime of PKR on single RNA molecule, PKR–Cy3 in imaging buffer A was injected (25 μ l min⁻¹) and after 1 min, imaging buffer A (no PKR) was injected into flow cell chamber (300 μ l min⁻¹, wash) and PKR survival lifetimes were monitored in real time (roughly 23 °C).

To measure the PKR occupancy on single-molecule ds-cRNA, imaging buffer B (imaging buffer A without PCA–PCD) was injected into flow cell chamber (300 μ l min⁻¹) and the photobleaching of PKR–Cy3 (laser 532 nm, 8 mW) was monitored in real time (roughly 23 °C).

Ribo-minus RNA-seq data analyses

First, RNA-seq datasets were treated via Trimmomatic⁷³ (parameters: PE -threads 16 -phred33 TruSeq3PE-2.fa:2:30:10 LEADING:3 TRAILING:3 SLIDINGWINDOW:4:15 MINLEN:30) to remove low quality bases and adapter sequences at both ends of reads. Next, paired reads were individually aligned to recombinant DNA sequences by Bowtie (v.0.12.9, parameters: -m 1 -k 1 -v 2 -p 12 -S) to remove reads from ribosomal RNAs, and then aligned to the reference genome (mouse mm10 and human hg38) with gene annotation (v.M25 of mouse and v.30 of human from GENCODE) by HISAT2 (ref. 74) (v.2.1.0, parameters: --known-splicesite-infile --no-softclip --rna-strandness RF --score-min L,-16,0 --mp 7,7 --rfg 0,7 --rdg 0,7 --max-seeds 20 -k 10 -t -p 12 -S). Gene expression of mRNAs was calculated by fragments per kilobase of transcript per million mapped reads with RSeQC (v.4.0.0, default parameters).

The expression of endogenous circRNAs was determined by CIRCexplorer3 (ref. 42). Briefly, unmapped reads after HISAT2 alignment were realigned to the mouse (mm10)/human (hg38) reference genome using TopHat-Fusion⁷⁵ (v.2.1.0, parameters --fusion-search --keep-fasta-order --bowtie1 --no-coverage-search) to identify reads from back-splicing junction sites. Then, CIRCexplorer3 (CLEAR) annotated the circRNAs' locations and expression with the gene annotation. FPBcirc, FPBlinear and CIRCscore were provided to evaluate and compare expression level of circRNAs and their cognate linear RNAs directly⁴². For mouse samples with different treatments, we calculated the mean of each circRNA in two repeats, then we selected 721 high-confidence circRNAs whose FPBcirc > 0.3 in D0 samples from WT or *Pkr*^{-/-} mouse. For samples from patients with psoriasis, all circRNAs were calculated from lesional and nonlesional skin samples of one patient.

Classification of the mRNA expression clusters

Gene expression changes that were less than twofold in two repeats of same time point were selected to analyze the gene expression pattern. The R packages Mfuzz (v.2.50) was used to cluster upregulated genes (more than a threefold change) in D1 compared to D0 of WT mouse time-series data. The KEGG pathway was enriched by genes in each cluster by clusterProfiler (v.4.6.2).

CircSHAPE–MaP data analyses

CircSHAPE–MaP libraries of circRNAs were prepared by the mixed PCR production. Each PCR production was added barcode at the 5' end (Supplementary Table 7). To separate each circRNA in the circSHAPE–MaP data, the barcodes were recognized by Cutadapt (v.3.10) with the parameter used before⁸.

After data separation, the circSHAPE–MaP data of each circRNA were analyzed by the optimized pipeline CIRCshapemapper v.2 (ref. 6) (<https://github.com/YangLab/circSHAPEmapper>). In brief, the target circRNA sequence and three circSHAPE–MaP datasets (NAI modified, denatured control and DMSO) were input into the pipeline. First, a new reference was generated by linking the overlapped sequences across the (back-) splicing junction from which came the theoretical PCR product of the target circRNA's circSHAPE–MaP. Then the index was built for local alignment by bowtie2 with new reference. After alignment, the mapped reads would be removed primer sequence and parsed to count mutation and coverage number of each site. Next, mutations were recounted according the original circRNA sequence. Finally, SHAPE reactivity was normalized after calculated with $((\text{Modified}_{\text{MutR}} - \text{Untreated}_{\text{MutR}}) / \text{Denatured}_{\text{MutR}})$.

The secondary structure modeling for circRNAs

The circRNA secondary structure was modeled by RNAfold (v.2.4.2) (parameter: -p -d2 --shape = SHAPE profile --shapeMethod = D --circ < circRNA.fa) with the SHAPE value generated by the CIRCshapemapper v.2.

In silico RNA secondary structures were predicted by RNAfold in the ViennaRNA package and drawn with StructureEditor.

The three-dimensional RNA structure modeling and docking with PKR

The 3D structure of EPIC was modeled by 3dRNA (v.2.0)⁷⁶ (<http://bio-phy.hust.edu.cn/3dRNA/>) with primary sequences and a modeled secondary structure (in the dot-bracket form) of EPIC. PKR structure was predicted by AlphaFold2 (<https://alphafold.ebi.ac.uk/entry/P19525>). The EPIC–PKR docking and 79bp–PKR docking were modeled by HDOCK³⁵.

Data analysis of smTIRF imaging

For studies involving RNA–Cy5–biotin and PKR–Cy3 in smTIRF experiments, fluorescent molecules (PKR–Cy3 and RNA–Cy5) in two channels were colocalized using a custom written MATLAB script. A 300 ms frame rate with 300 ms laser exposure time was used to examine PKR on RNA, kymographs were generated along the RNA by a kymograph plug-in in ImageJ (J. Rietdorf and A. Seitz, EMBL Heidelberg). To determine the frequency of PKR on RNA, single-molecule videos were recorded for 2 min, Cy3 and Cy5 channels were merged and colocalized molecules with a minimum lifetime of 3 s were counted as binding events (N_{binding}). Following real-time single-molecule recording, the number of RNA molecules (N_{RNA}) was determined by Cy5 dots. The frequencies of RNA binding by PKR (F_{binding}) were calculated:

$$F_{\text{binding}} = N_{\text{binding}} / N_{\text{RNA}}$$

Following the real-time single-molecule recording, the number of stable and/or transient binding PKR to single RNA molecules was counted (N_{stable} and $N_{\text{transient}}$, respectively). The stable and transient fractions (F_{stable} and $F_{\text{transient}}$) were calculated:

$$F_{\text{stable}} = N_{\text{stable}} / N_{\text{binding}}$$

$$F_{\text{transient}} = N_{\text{transient}} / N_{\text{binding}}$$

To plot the survival lifetime of PKR on RNAs, the number of PKR–Cy3 at the beginning of each video was set to 1. The beginning of wash (injection of imaging buffer A) was set to 0 s, the binding time of a

single PKR molecule (T_{binding}) was calculated from wash to dissociation and quantified in 5-s time bins.

To calculate the PKR-Cy3 photobleaching steps on single EPIC molecule, single-molecule videos were recorded for 20 min. Photobleaching step analysis was performed using the quickPBSA package or hidden Markov model³².

Statistical analysis

For the statistical significance and sample size of all graphs, please see figure legends and Methods for details. For epidermal thickness measurement, means were calculated based on five random site measurements by ImageJ in three different regional images of independent biological individuals, respectively.

Display items

The images of mice, syringes and other icons in Figs. 3a and 4a were created with BioRender.com.

Materials availability

All unique and/or stable reagents generated in this study are available from the lead contact under a material transfer agreement with CEMCS, CAS. Requests should be submitted by email to L.-L.C.

Reporting summary

Further information on research design is available in the Nature Portfolio Reporting Summary linked to this article.

Data availability

All data supporting the findings of this study are available in the paper, Source Data and at <https://doi.org/10.17632/zfm9kmfghs.2> (ref. 77). All sequencing data reported in this paper have been deposited in the Gene Expression Omnibus (GEO). High-throughput datasets generated in this study are available at GSE248680 (ref. 78), including circSHAPE-MaP data (GSE248679) and mouse RNA-seq data (IMQ-treated *Pkr*^{-/-} mouse data, GSE248678; mouse spleens delivered EPIC-LNPs data, GSE253346); published RNA-seq data of patients with psoriasis can be downloaded from GEO under accession number GSE121212 (ref. 79). Source data are provided with this paper.

Code availability

This paper does not report original code. Any additional information required to reanalyze the data reported in this paper is available from the lead contact on request.

References

67. Guimaraes, C. P. et al. Site-specific C-terminal and internal loop labeling of proteins using sortase-mediated reactions. *Nat. Protoc.* **8**, 1787–1799 (2013).
68. Donovan, J., Rath, S., Kolet-Mandrikov, D. & Korennykh, A. Rapid RNase L-driven arrest of protein synthesis in the dsRNA response without degradation of translation machinery. *RNA* **23**, 1660–1671 (2017).
69. Xiao, M. S. & Wilusz, J. E. An improved method for circular RNA purification using RNase R that efficiently removes linear RNAs containing G-quadruplexes or structured 3' ends. *Nucleic Acids Res.* **47**, 8755–8769 (2019).
70. Matsui, T., Tanihara, K. & Date, T. Expression of unphosphorylated form of human double-stranded RNA-activated protein kinase in *Escherichia coli*. *Biochem. Biophys. Res. Commun.* **284**, 798–807 (2001).
71. Smola, M. J., Rice, G. M., Busan, S., Siegfried, N. A. & Weeks, K. M. Selective 2'-hydroxyl acylation analyzed by primer extension and mutational profiling (SHAPE-MaP) for direct, versatile and accurate RNA structure analysis. *Nat. Protoc.* **10**, 1643–1669 (2015).

72. Senavirathne, G. et al. Widespread nuclease contamination in commonly used oxygen-scavenging systems. *Nat. Methods* **12**, 901–902 (2015).
73. Bolger, A. M., Lohse, M. & Usadel, B. Trimmomatic: a flexible trimmer for Illumina sequence data. *Bioinformatics* **30**, 2114–2120 (2014).
74. Kim, D., Langmead, B. & Salzberg, S. L. HISAT: a fast spliced aligner with low memory requirements. *Nat. Methods* **12**, 357–360 (2015).
75. Kim, D. & Salzberg, S. L. TopHat-Fusion: an algorithm for discovery of novel fusion transcripts. *Genome Biol.* **12**, R72 (2011).
76. Zhang, Y., Wang, J. & Xiao, Y. 3dRNA: 3D structure prediction from linear to circular RNAs. *J. Mol. Biol.* **434**, 167452 (2022).
77. Othniel, J. "doi: 10.17632/j6fmfjrc5y.1", Mendeley Data, V1. *Mendely Data* <https://doi.org/10.17632/94jg7jkt6n.1> (2020).
78. Guo, S. K. et al. *Therapeutic Application of Circular RNA Aptamers in a Mouse Model of Psoriasis* (Gene Expression Omnibus, 2024); <http://www.ncbi.nlm.nih.gov/geo/query/acc.cgi?acc=GSE248680>
79. Weidinger S., Rodriguez E., Tsoi L. C. & Gudjonsson J. *Atopic Dermatitis, Psoriasis and Healthy Control RNA-seq Cohort* (Gene Expression Omnibus, 2019); <https://www.ncbi.nlm.nih.gov/geo/query/acc.cgi?acc=GSE121212>

Acknowledgements

We thank F. Nan at Shanghai Institute of Materia Medica for support in LNPs, and the Chen laboratory members for critical discussion. This work was supported by National Key R&D Program of China (grant no. 2021YFA1300501), Strategic Priority Research Program of the Chinese Academy of Science (grant no. XDB0570000) and Science and Technology Commission of Shanghai Municipality (STCSM) (grant nos. 23DX1900100 and 23DX1900101) to L.-L.C.; National Natural Science Foundation of China (NSFC) (grant no. 31925011), National Key R&D Program of China (grant nos. 2021YFA1300503 and 2019YFA0802804) and STCSM (grant nos. 23DX1900102 and 23JS1400300) to L.Y.; NSFC (grant no. 32371349) and Shanghai Rising-Star Program (grant no. 23QA1410200) to C.-X.L.; China National Postdoctoral Program for Innovative Talents (grant nos. BX20220298 and BX20220077) and Shanghai Postdoctoral Excellence Program (grant nos. 2022757 and 2022728) to X.W. and F.N. D.P. acknowledges the support from the European Research Council (advance grant no. 101055029). This work has been supported by the New Cornerstone Science Foundation through the New Cornerstone Investigator Program and the XPLOER PRIZE.

Author contributions

L.-L.C. supervised and conceived the project. S.-K.G., C.-X.L., Y.-F.X. and X.W. designed and performed experiments. F.N. performed computational analyses, supervised by L.Y. Y.H., S.L., L.L., E.K. and N.A. formulated LNPs, supervised by D.P. and L.-L.C. R.S. and S.P. provided samples from patients with psoriasis, supervised by T.C. C.L. helped with smTIRF experiments, supervised by J.L. J.W. generated the next-generation sequencing library. S.N. and M.-Y.W. helped with biochemical and mice experiments. L.-L.C., S.-K.G., C.-X.L., Y.-F.X., X.W. and F.N. wrote the paper with input from all authors. All authors read and approved the manuscript.

Competing interests

L.-L.C., S.-K.G., C.-X.L., S.L. and Y.-F.X. are named as inventors on patents related to circRNA held by CAS CEMCS. L.-L.C. is a scientific co-founder of RiboX Therapeutics. D.P. receives licensing fees (to patents on which he was an inventor) from, invested in, consults (or on scientific advisory boards or boards of directors) for, lectured (and received a fee) or conducts sponsored research at TAU for the following entities: ART Biosciences, BioNtech SE, Earli Inc., Kernal Biologics, Geneditor Biologics, Newphase Ltd,

NeoVac Ltd, RiboX Therapeutics, Roche, SirTLabs Corporation and Teva Pharmaceuticals Inc.

Correspondence and requests for materials should be addressed to Ling-Ling Chen.

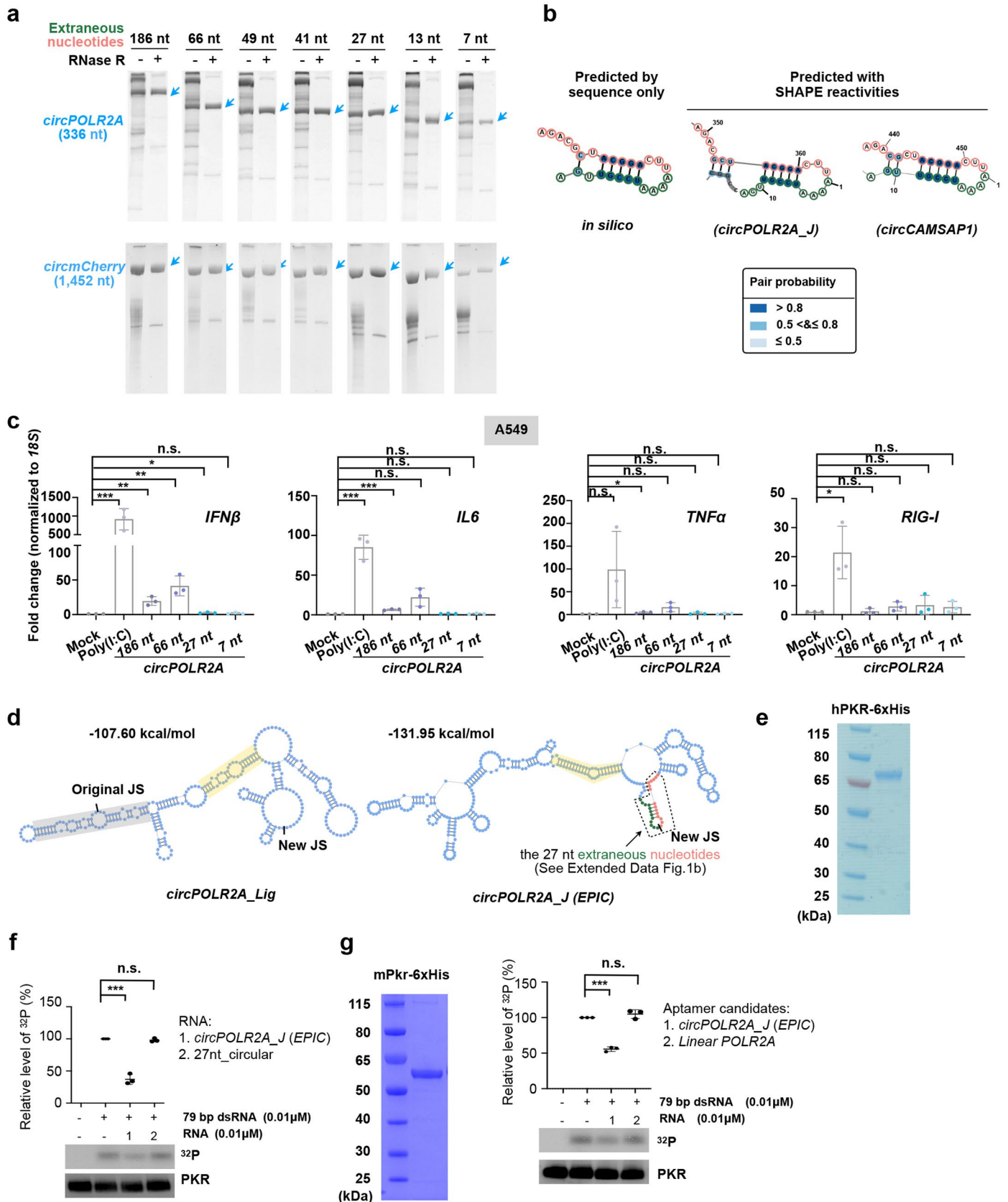
Additional information

Extended data is available for this paper at <https://doi.org/10.1038/s41587-024-02204-4>.

Peer review information *Nature Biotechnology* thanks the anonymous reviewers for their contribution to the peer review of this work.

Supplementary information The online version contains supplementary material available at <https://doi.org/10.1038/s41587-024-02204-4>.

Reprints and permissions information is available at www.nature.com/reprints.

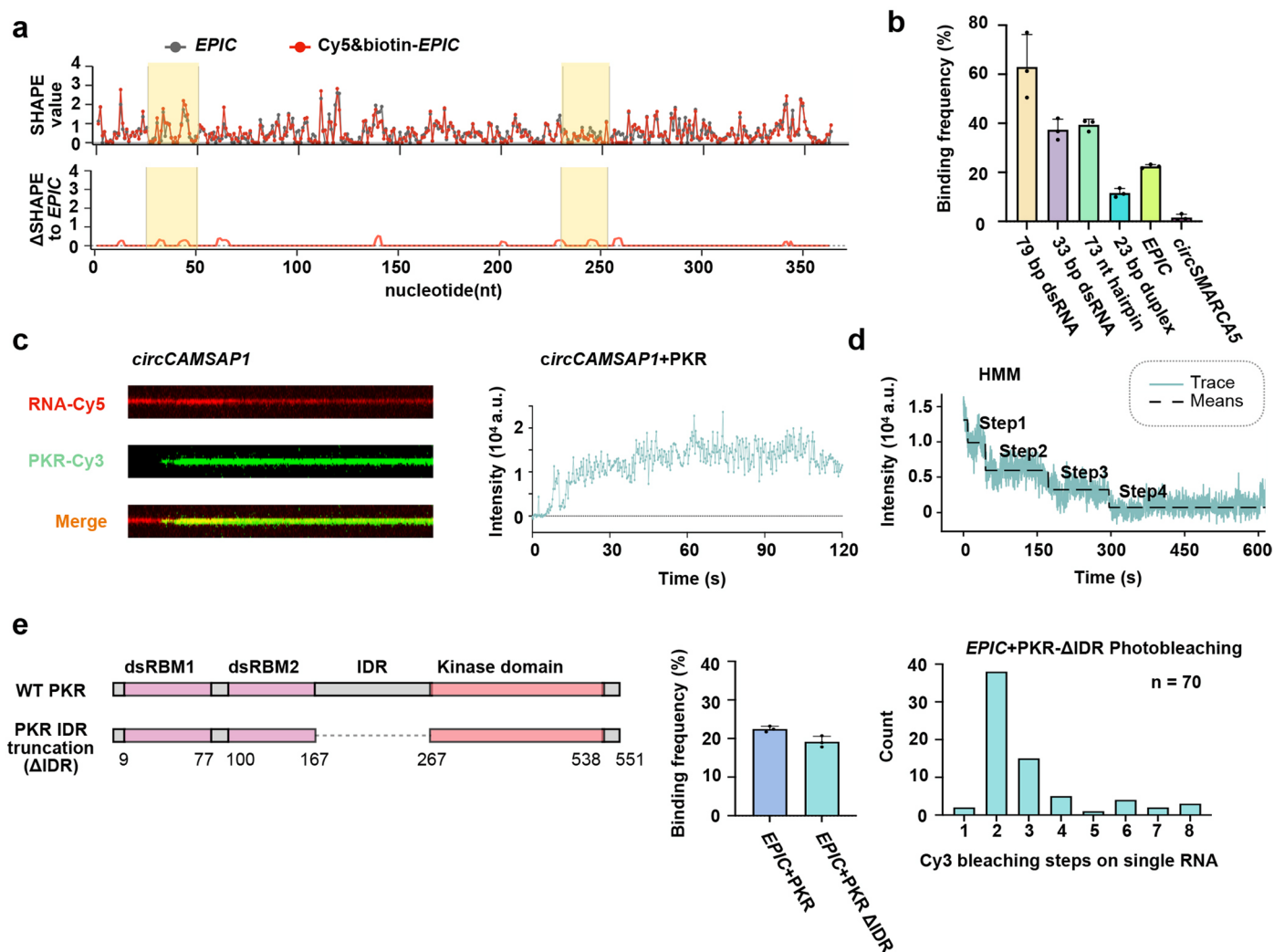


Extended Data Fig. 1 | See next page for caption.

Extended Data Fig. 1 | EPIC synthesized by optimized strategy preserves its characteristics in minimized immunogenicity and folding status.

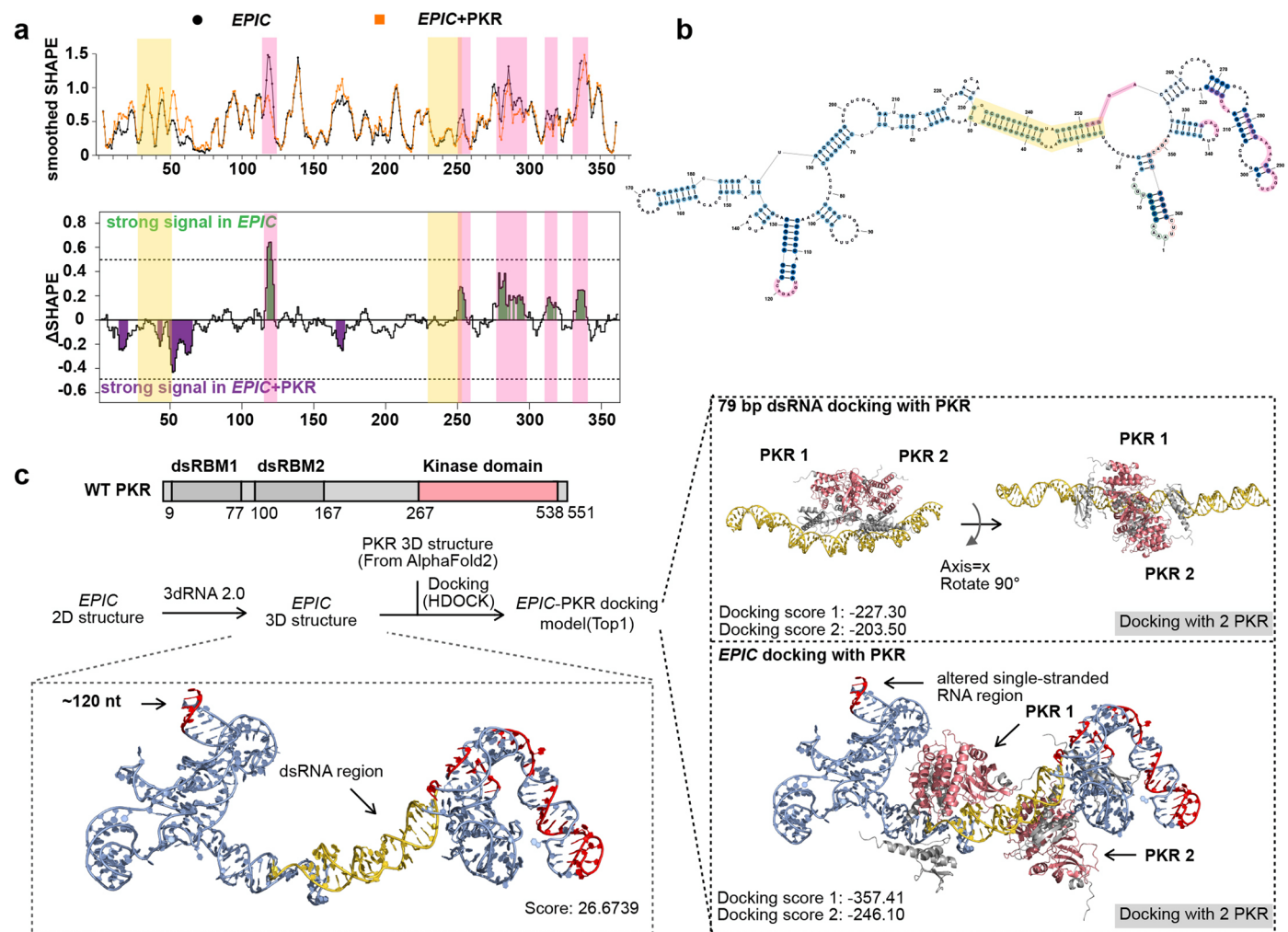
(a) Examination of circularization efficiency of two circular RNAs (circPOLR2A, 336 nt; circmCherry, 1452 nt) using *Anabaena* tRNA^{Leu}-derived PIE with varied lengths of extraneous nucleotides. Circularized RNA products are analyzed with denaturing PAGE, bands of RNA circles are verified with RNase R and marked with blue arrows. Representative results are shown from three replicates. Gels of each replicate are processed in parallel. (b) The 27 nt extraneous sequence tend to form stem-loop alone at the JS, independent of cargo sequences by predictions of *in silico* and SHAPE-MaP. (c) Ana_PIE_27nt version results in minimal induction of inflammatory factors. The same amounts of circular POLR2A (200 ng for each sample) with varied lengths of extraneous nucleotides were transfected into A549 cells. Relative expression of inflammatory factors after 6 hours transfection were examined by RT-qPCR. $n = 3$ biological repeats. (d) Secondary structures of

circPOLR2A_Lig and circPOLR2A_J (EPIC). Left, the original and new junction sites are indicated in the secondary structure of circPOLR2A_Lig⁸. Right, the secondary structure of circPOLR2A_J (EPIC), in which the 27 nt extraneous sequences forms a stable step-loop. The predicted imperfect duplex regions are marked with gray and yellow shadows. (e) Human PKR protein purified from *E. coli* is shown by SDS-PAGE and Coomassie Blue staining. (f) The 27 extra nucleotides RNA circle doesn't suppress PKR phosphorylation. Purified PKR (0.6 μ M) is activated by 79 bp dsRNA (0.01 μ M) *in vitro*, which is shown by autoradiography using γ -³²P-ATP. 0.01 μ M of RNA circles are used in the assays. (g) EPIC suppresses mouse PKR phosphorylation efficiently. Left, purified mouse PKR protein is shown by SDS-PAGE and Coomassie Blue staining. Right, the activation of mPkr (0.6 μ M) by 79 bp dsRNA (0.01 μ M) *in vitro*, is inhibited by EPIC (0.01 μ M). **c, f** and **g**: n.s., $p > 0.05$, * $p < 0.05$, ** $p < 0.005$, *** $p < 0.001$, two-tailed student's *t* test, data are shown as mean \pm SD.



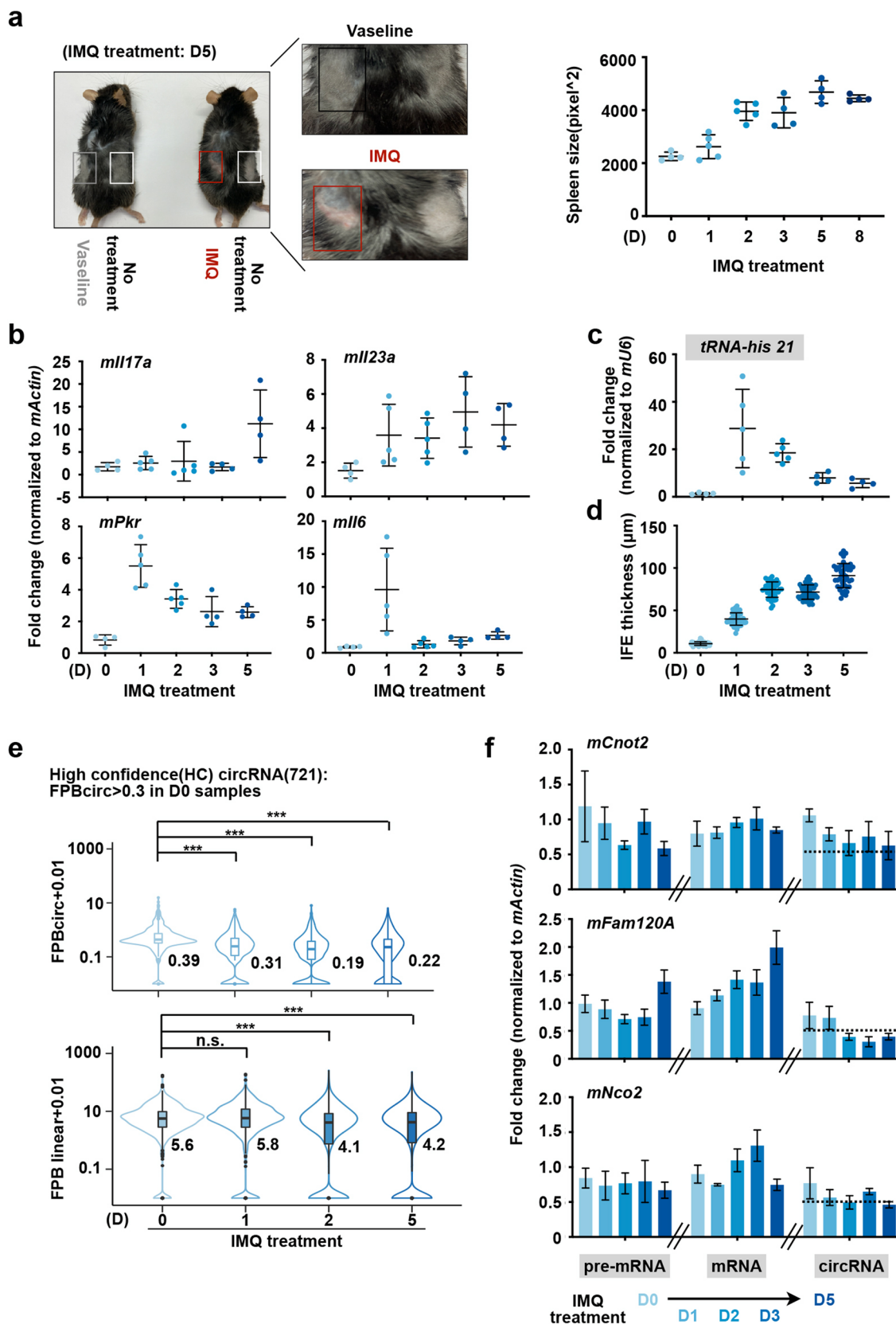
Extended Data Fig. 2 | Stable interactions of ds-cRNAs and PKR resolved by single molecule imaging. (a) Cy5 and biotin labeling did not alter the EPIC conformation in general. SHAPE reactivity of each group was quantified at the single nucleotide resolution, and Δ SHAPE was calculated accordingly and plotted in absolute values. (b) The binding frequency between PKR and examined RNAs by smTIRF. The numbers of RNAs counted in each column with three independent replicates: 79 bp dsRNA, $n = 265, 108, 157$; 33 bp dsRNA, $n = 204, 179, 135$; 73 nt hairpin RNA, $n = 207, 281, 394$; 23 bp duplex RNA, $n = 178, 277, 363$; EPIC, $n = 134, 150, 178$; circSMARCA5, $n = 67, 101, 78$. The binding frequency of PKR on each RNA: 79 bp dsRNA, 62.9%; 33 bp dsRNA, 37.3%; 73 nt hairpin RNA, 39.4%; 23 bp duplex RNA, 11.6%; EPIC, 22.4%; circSMARCA5, 1.5%. Data are shown as mean \pm SD. (c) A similar robust binding between PKR and circCAMSAP1.

Left, representative kymograph of circCAMSAP1-Cy5 binding with PKR-Cy3 in separated and merged channels. Right: quantification of the PKR-Cy3 intensity on a single RNA molecule within 120 s. (d) HMM has been applied to analysis single-step photobleaching data. Trace line represents raw PKR-Cy3 trajectory of one exemplary molecule recorded by smTIRF. Means line represents the idealized trajectory determined by HMM. (e) The interaction between EPIC and PKR- Δ IDR is similar with WT PKR. Left, the construction of WT PKR and PKR- Δ IDR. Middle, the binding frequency between EPIC and PKR (or PKR- Δ IDR). The numbers of RNAs counted in each column with three independent replicates: PKR, $n = 287, 201, 350$; PKR- Δ IDR, $n = 237, 371, 299$. Data are shown as mean \pm SD. Right, the number of PKR- Δ IDR binding on single EPIC is calculated based on the step analysis of PKR- Δ IDR-Cy3 photobleaching. $n =$ number of events examined.



Extended Data Fig. 3 | Chemical probing and docked structure reveal the potential binding mode between one EPIC with two PKR molecules. (a) The SHAPE signal difference (Δ SHAPE value) of EPIC with or without PKR protein in vitro. Top, SHAPE reactivity of each group is quantified. Bottom, Δ SHAPE value of EPIC with or without PKR protein in vitro. Yellow shadow indicates the nucleotides of 23 bp imperfect dsRNA-region. Regions with significant SHAPE augment upon PKR binding are in purple, regions with reduced SHAPE signals upon PKR binding are in green and marked by pink shadow. (b) Predicted secondary structure of EPIC based on circSHAPE-MaP signals. Of note, EPIC

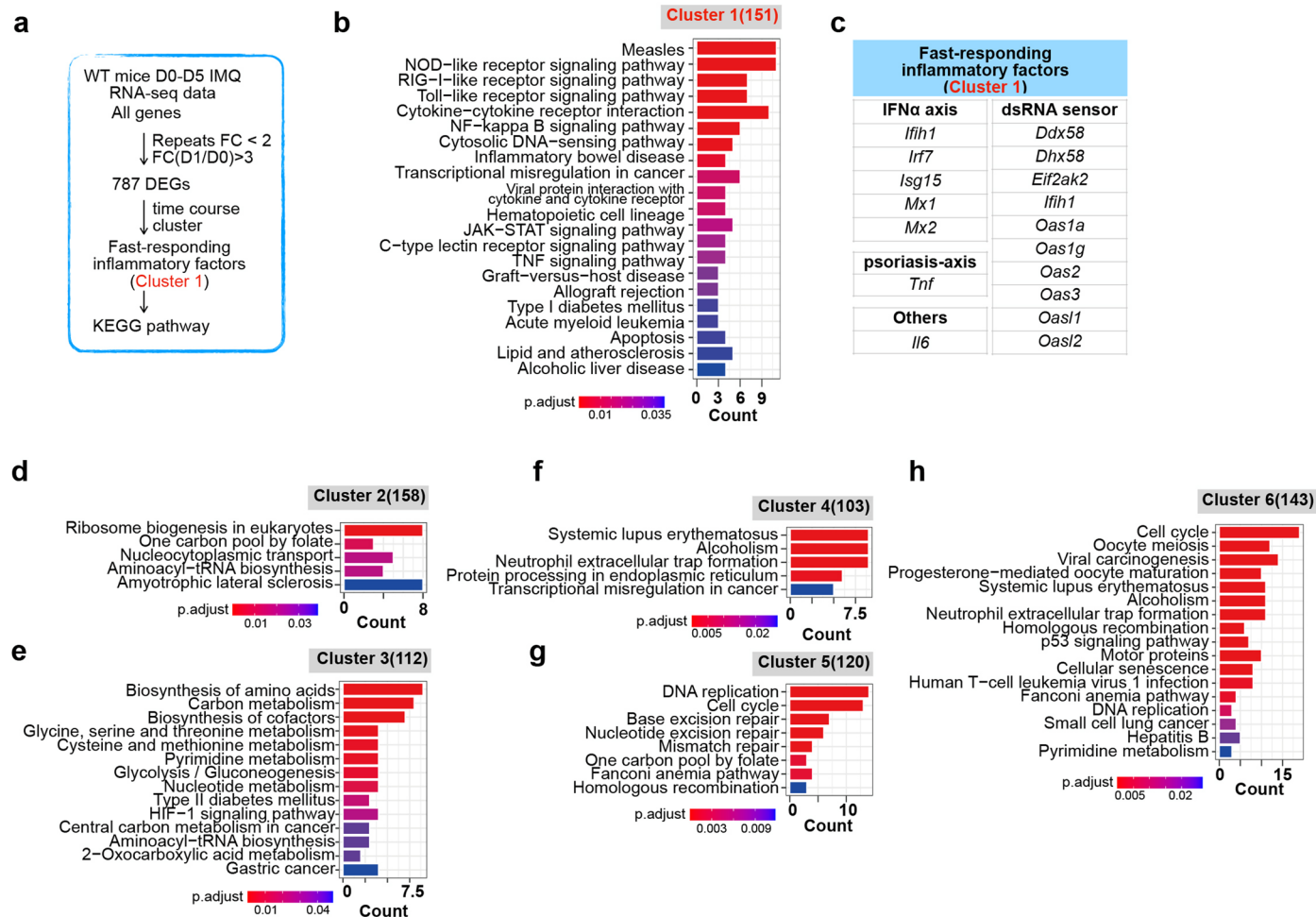
contains one imperfect dsRNA region sufficient for PKR binding (yellow shadow, 23 bp). The heavy pink lines denote the altered NAI accessibility in EPIC upon PKR addition. (c) Predicted EPIC structure and the binding with PKR. Top left, domains of PKR and the schematic pipeline for docking EPIC on PKR. Bottom left, the most possible 3D structure of EPIC predicted by 2D structure with circSHAPE-MaP signal. Right, the binding modes of 79 bp dsRNA (top) and EPIC (bottom) docked with two PKR molecules predicted by AlphaFold2. The 23 bp imperfect dsRNA region is labeled in yellow, and the nucleotides with altered SHAPE reactivities upon PKR binding are labeled in red.



Extended Data Fig. 4 | See next page for caption.

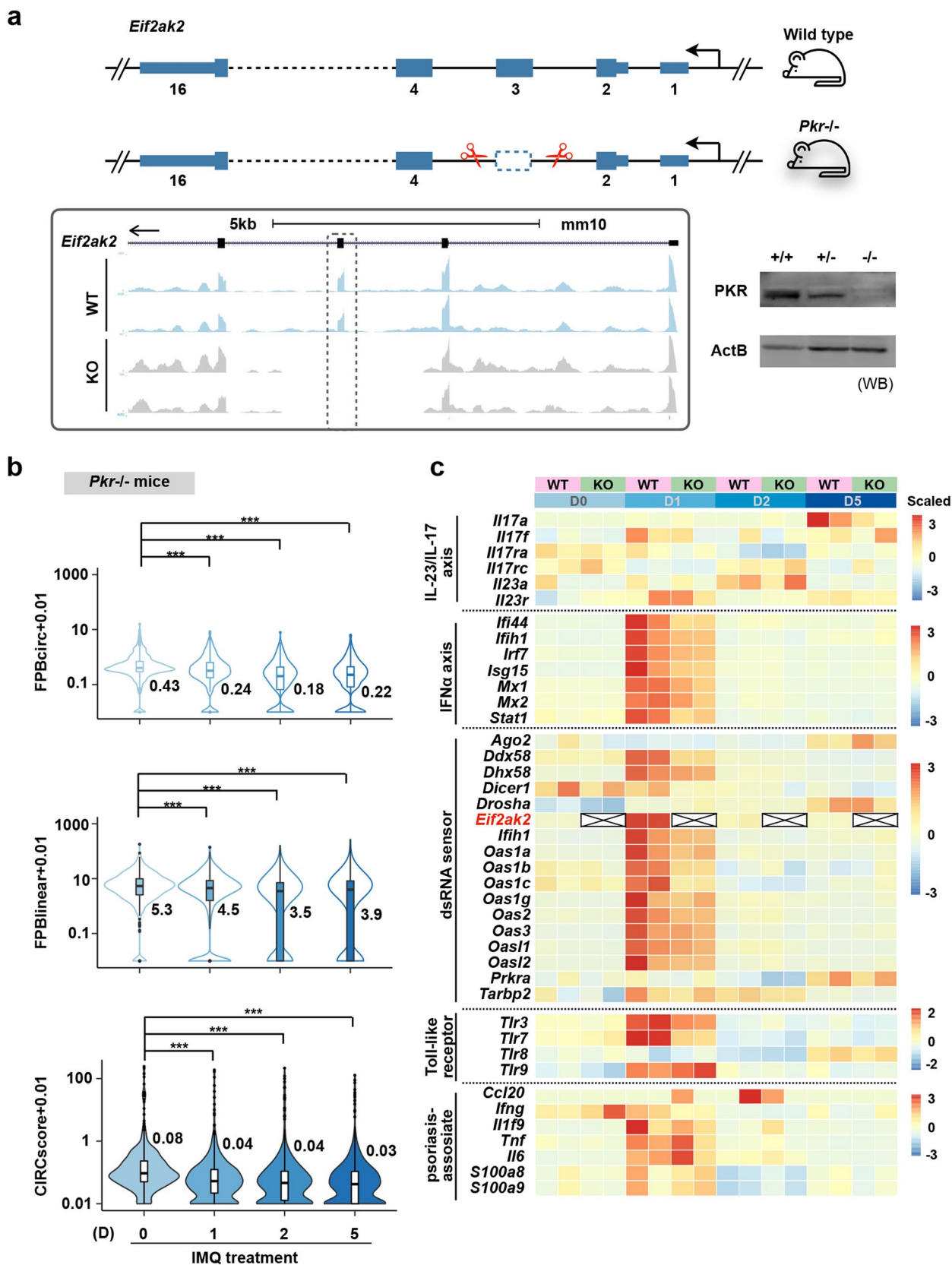
Extended Data Fig. 4 | CircRNAs are globally degraded at the initial inflammation stage in IMQ-induced psoriasis mice model. (a) Phenotypes of IMQ-induced psoriasis mice model. Left, representative image of mice showing skin inflammation after IMQ treatment on dorsal skin, compared to Vaseline treatment or blank control. Right, quantification of the spleen size at indicated time points upon IMQ treatment. $n = 4$ or 5 animals in each group. (b) Increased expression of psoriasis-related genes with distinct patterns. Relative expression levels of the psoriasis-related genes (mIl17a and mIl23a), mPkr and mIl6 were examined by RT-qPCR. The expression is normalized to DO expression. $n = 4$ or 5 animals in each group and mActin is used as an internal control for normalization.

(c) Activation of RNase L was measured by RT-qPCR combined with RctB ligation. (d) Increased epidermis thickness of dorsal skins from IMQ-treated mice. $n = 3$ animals in each group. (e) Expression level of 721 HC circRNAs and their cognate linear RNAs in IMQ treated mice. The value of each time point is the mean from two repeats, and each repeat includes 2 biologically independent animals. Data are shown as median and IQR. Wilcoxon rank-sum test, *** $p < 0.001$. (f) Validation of randomly selected circRNAs, their cognate mRNAs and pre-mRNAs at indicated time points in IMQ treated mice. Expression of these RNAs were examined by RT-qPCR and normalized to mActin. Data are shown as mean \pm SD.



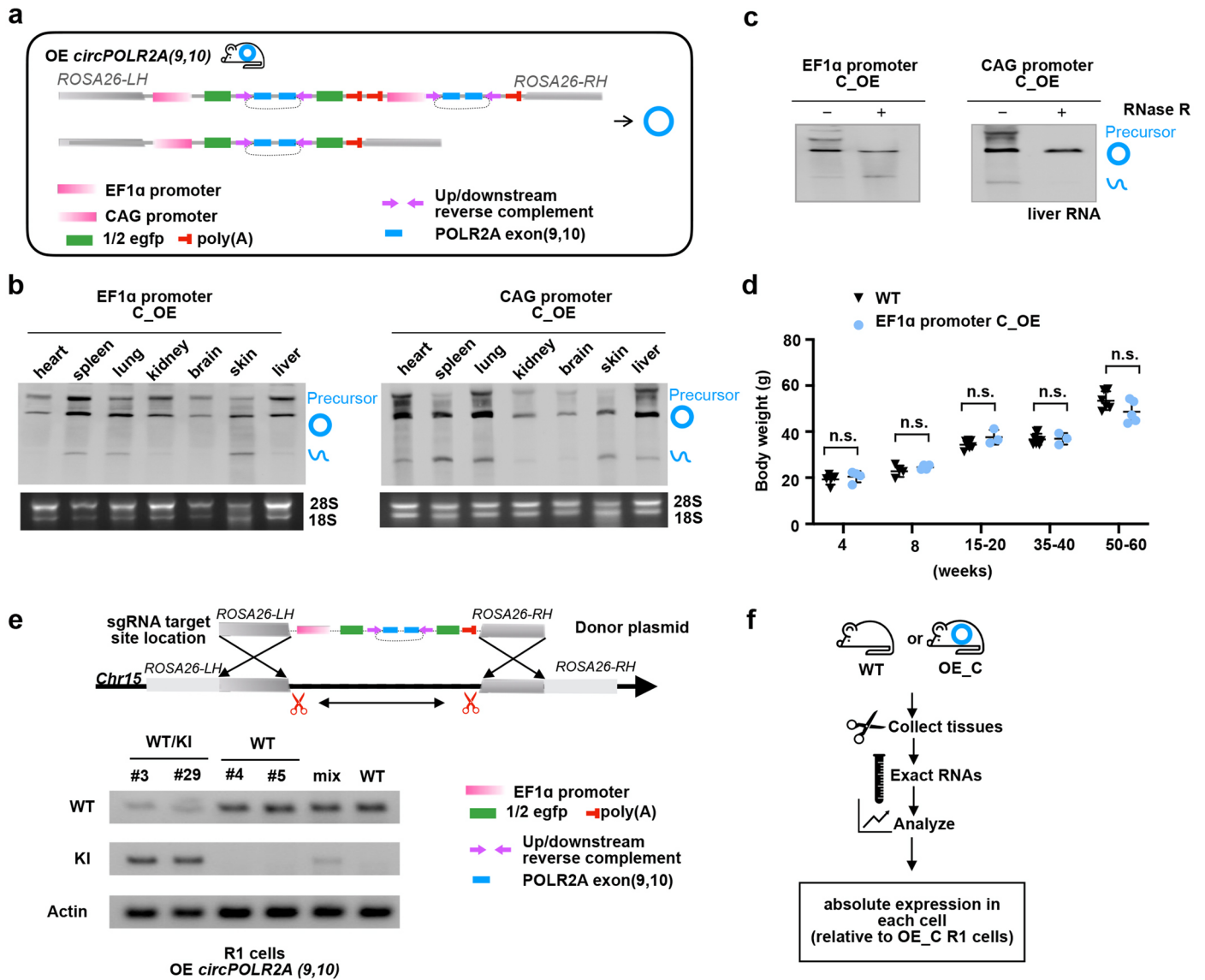
Extended Data Fig. 5 | Enrichment analyses reveal up-regulated pathways in the initial stage of psoriasis pathogenesis. (a) Schematic of clustering the fast-responding inflammatory factors including PKR. 787 DEGs are defined as over threefold up-regulation at D1 compared to D0 in two biological repeats. All DEGs are performed the KEGG pathway enrichment analysis. (b) The KEGG analyses of 151 genes from Cluster 1. (c) A short list of the most enriched genes of Cluster

1 which belong to the IFN α signaling pathways and the dsRNA-sensors related genes. (d)-(h) The enriched KEGG pathways of genes from the other 5 clusters of distinct gene expression patterns in IMQ-induced psoriasis mice model. b, d, e, f, g, h: all pathways are selected according p.adjust < 0.05 and the pathways related to viral or bacterial infection are not shown in Cluster 1.



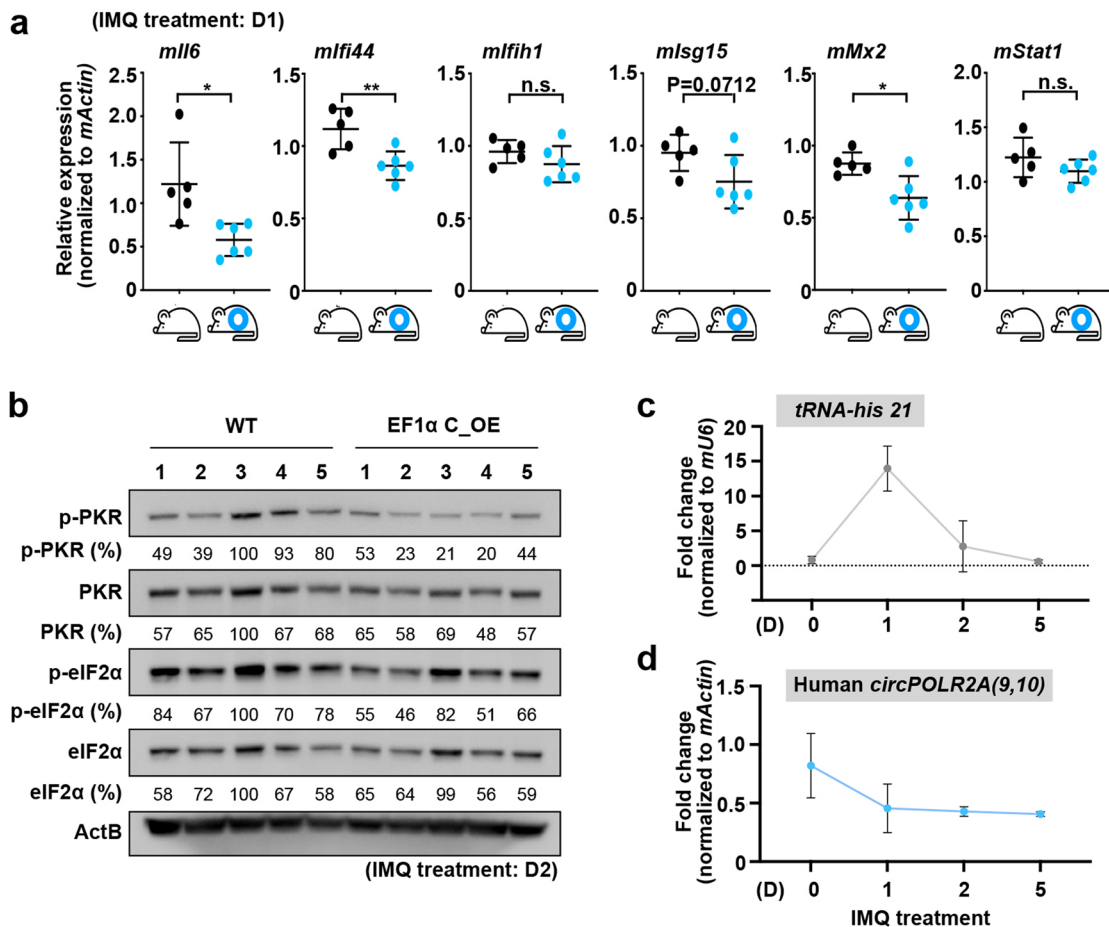
Extended Data Fig. 6 | Generation of *Pkr*^{-/-} mice. (a) Generation of *Pkr*^{-/-} mice by CRISPR/Cas9. Top, the schematic of generating *Pkr*^{-/-} mice. Bottom left, the wiggle track of RNA-seq data of total RNAs collected from WT and *Pkr*^{-/-} mice spleens. Bottom right, WB verification of mPkr loss. (b) The expression of circRNAs and their cognate linear RNAs in *Pkr*^{-/-} mice with IMQ treatment. FPBcirc values (top), FPBlinear value (middle) and CIRCscore (bottom) of 721 HC circRNAs in each indicated time points, related to Fig. 3c and Extended Data Fig. 4e.

Each corresponding group is calculated mean from two biological repeats, and each repeat with 2 biologically independent animals. Data are shown as median and IQR. Wilcoxon rank-sum test, ****p* < 0.001. (c) Heatmap of selected categories of psoriasis-related gene expression from the IMQ-treated spleens of *Pkr*^{-/-} and paired WT mice. Each repeat includes two biologically independent animals. The expression of each gene is scaled by z-score and each category is shown in the same scale bar, indicated by intervals.



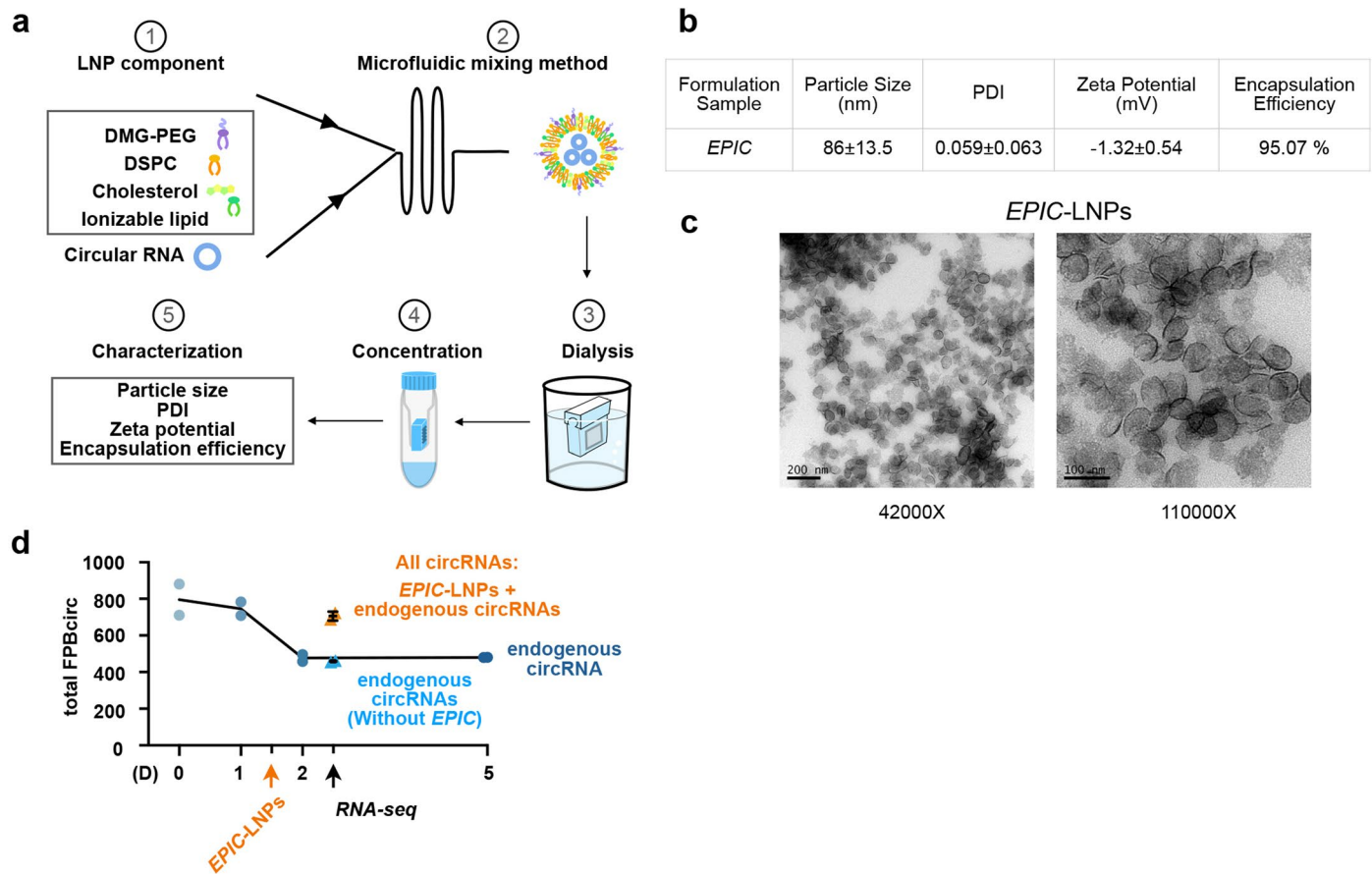
Extended Data Fig. 7 | Generation of the in vivo over-expressed human circPOLR2A (9,10) mice model (C_OE mice). (a) Schematic of generating C_OE mice carrying the circPOLR2A (9,10) constitutive expression cassette. (b) NB analysis showed constitutive human circPOLR2A (9,10) production in all examined tissues in the EF1α promoter and CAG promoter driven C_OE mice. (c) NB analysis confirmed the expression of human circPOLR2A (9,10) in the liver of EF1α and CAG C_OE mice, respectively. (d) EF1α C_OE mice exhibited

unobservable abnormalities compared to WT mice, here showing the weight analysis of WT and the littermate EF1α C_OE mice from 4 to 60 weeks. Each dot represents one individual animal ($n \geq 3$) at each examined time point. n.s., $p > 0.05$, two-tailed student's t test, data are shown as mean \pm SD. (e) Generation of the *in vivo* over-expressed human circPOLR2A (9,10) R1 cell lines. (f) Schematic of calculating the copy number of human circPOLR2A (9,10) in C_OE mice, relative to OE_C R1 cells in e.



Extended Data Fig. 8 | In vivo over-expression of the human circPOLR2A (9, 10) mitigates the IMQ-induced psoriasis pathogenesis. (a) Human circPOLR2A (9,10) dampens the expression of inflammatory factors in IMQ mice. Relative expression of representative IFN α signaling pathways in C_OE mice ($n = 6$), compared to WT mice ($n = 5$) on D1, examined by RT-qPCR. n.s., $p > 0.05$, * $p < 0.05$, ** $p < 0.005$, two-tailed student's t test, data are shown as mean \pm SD. (b) Human

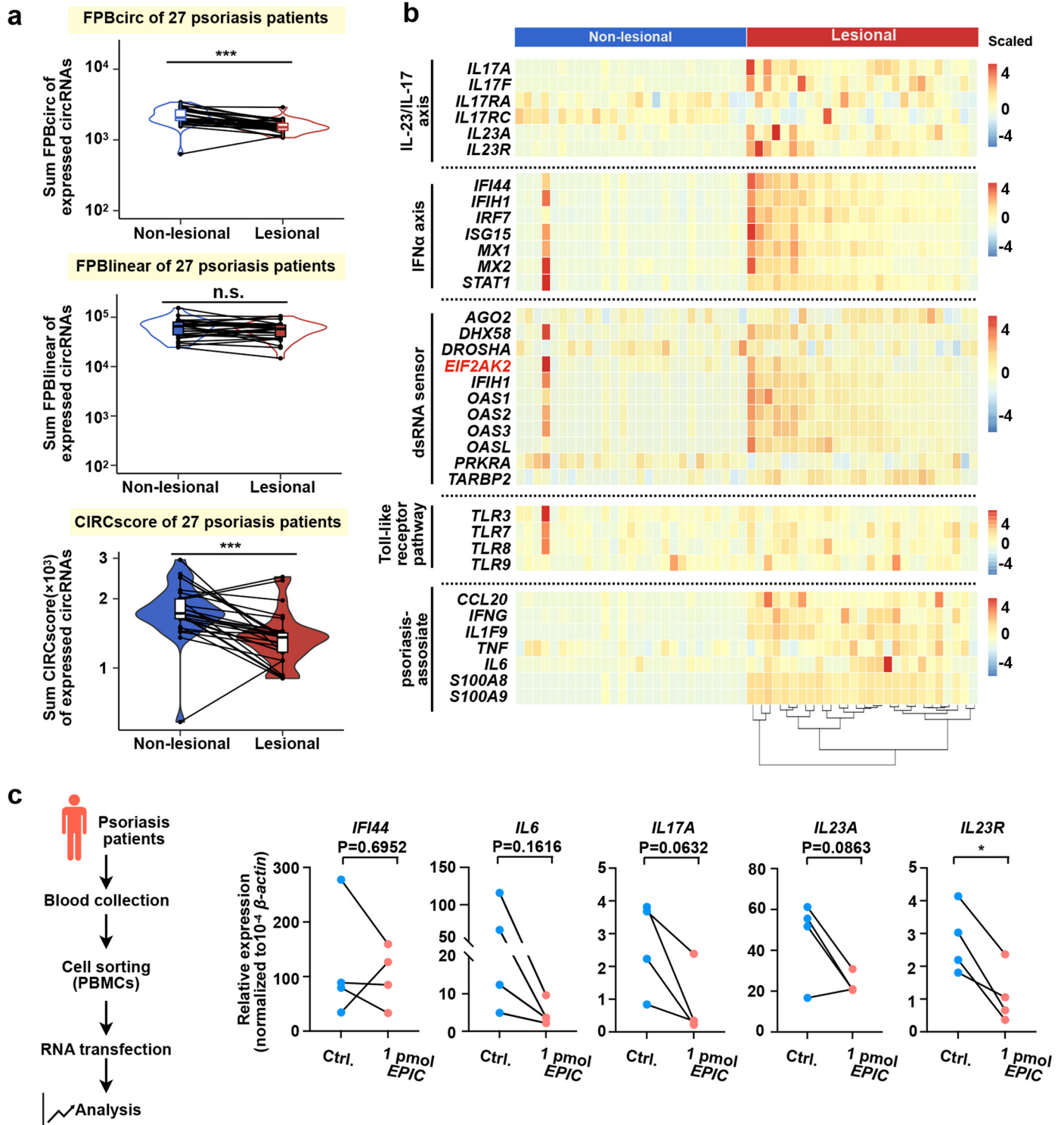
circPOLR2A (9,10) dampens PKR activation in IMQ mice. PKR activation kinetics were analyzed in C_OE and WT mice on D2, ActB was used as the internal control. (c) RNase L activation on D1 led to reduced circPOLR2A (9,10) in C_OE mice. (d) Relative expression levels of the circPOLR2A (9,10) were examined by RT-qPCR in IMQ mice. The expression of circPOLR2A (9,10) is normalized to D0 and *mActin* is used as an internal control for normalization.



Extended Data Fig. 9 | Ds-cRNAs are encapsulated by ionizable LNPs.

(a) Schematic of a microfluidic mixing preparation of circular RNA-encapsulated ionizable-based LNPs. (b) Physicochemical characterization of ds-cRNA-encapsulated ionizable-based LNPs. The particle size, PDI, Zeta potential and encapsulation efficiency of EPIC-LNPs were measured in three replicates. Data are shown as mean \pm SD. (c) Transmission electron micrographs of EPIC-LNPs. (d) Examination of endogenous circRNA expression upon ds-cRNA treatment

by RNA-seq. Blue dots, quantification of total RNAs from spleens of IMQ mice without EPIC-LNPs. Orange triangles, quantification of total RNAs from spleens at 24 hrs post i.v. of 150 pmol EPIC-LNPs at D1.5 IMQ mice; of note, EPICs were counted by FPBcirc in these samples. Blue triangles, quantification of total endogenous RNAs from same samples shown by Orange triangles, but leaving out EPICs during calculation by FPBcirc. EPIC-LNPs treatment restored the reduced endogenous circRNA almost to the D0 level.



Extended Data Fig. 10 | Expression of fast-responding inflammatory factors is elevated in psoriasis patients and the ds-cRNA treatment is beneficial in patient-derived PBMCs. (a) The expression of circRNAs is reduced in the lesional skin samples, compared to the non-lesional skin samples. Total expression level of circRNAs from lesional and non-lesional skin samples derived from 27 psoriasis patients^{19,20} are analyzed. Top, total FPBcirc values of all circRNAs; median, total FPBlinear values of all circRNAs cognate linear RNAs; bottom, total CIRCscore values of all circRNAs. Wilcoxon rank-sum test,

n.s., $p > 0.05$, *** $p < 0.001$. (b) Heatmap of the psoriasis-related genes of lesional and non-lesional skin in psoriasis patients. The expression level of each gene is scaled by z-score and each category is shown in the same scale bar, indicated by intervals. (c) EPIC-LNPs suppresses the expression of psoriatic signature genes in PBMCs isolated from psoriasis patients. 1 pmol of EPIC was delivered into roughly 10⁶ cells. Each dot represents one patient sample. n.s., $p > 0.05$, * $p < 0.05$, paired student's t test.

Reporting Summary

Nature Portfolio wishes to improve the reproducibility of the work that we publish. This form provides structure for consistency and transparency in reporting. For further information on Nature Portfolio policies, see our [Editorial Policies](#) and the [Editorial Policy Checklist](#).

Statistics

For all statistical analyses, confirm that the following items are present in the figure legend, table legend, main text, or Methods section.

n/a | Confirmed

- The exact sample size (n) for each experimental group/condition, given as a discrete number and unit of measurement
- A statement on whether measurements were taken from distinct samples or whether the same sample was measured repeatedly
- The statistical test(s) used AND whether they are one- or two-sided
Only common tests should be described solely by name; describe more complex techniques in the Methods section.
- A description of all covariates tested
- A description of any assumptions or corrections, such as tests of normality and adjustment for multiple comparisons
- A full description of the statistical parameters including central tendency (e.g. means) or other basic estimates (e.g. regression coefficient) AND variation (e.g. standard deviation) or associated estimates of uncertainty (e.g. confidence intervals)
- For null hypothesis testing, the test statistic (e.g. F , t , r) with confidence intervals, effect sizes, degrees of freedom and P value noted
Give P values as exact values whenever suitable.
- For Bayesian analysis, information on the choice of priors and Markov chain Monte Carlo settings
- For hierarchical and complex designs, identification of the appropriate level for tests and full reporting of outcomes
- Estimates of effect sizes (e.g. Cohen's d , Pearson's r), indicating how they were calculated

Our web collection on [statistics for biologists](#) contains articles on many of the points above.

Software and code

Policy information about [availability of computer code](#)

Data collection

smTRIF images were acquired with Olympus IX73, EMCCD camera (iXon Ultra 897, Andor, OptoSplit II emission image splitter, Cairn Research). High-throughput sequencing libraries were sequenced with 150 nt paired-end on Illumina NovaSeq. qRT-PCR data was collected by ABI-Quantstudio 6 Flex Real-Time PCR system, 384-well.

Data analysis

For smTRIF analyses, Minerva, Cornell SPARTAN (a custom written MATLAB script) and ImageJ were used. RNA-seq data was trimmed low quality bases and adapter by Trimmomatic, then rRNA sequences were removed in RNA-seq data by Bowtie 0.12.9. Clean data was aligned to genome reference (mm10/hg38) via HISAT2(v2.1.0). Gene expression of mRNAs was calculated via FPKM by RSeQC 4.0.0 and the endogenous circRNAs were identified and quantified by CIRCexplorer3/CLEAR (<https://github.com/YangLab/CLEAR>). The mRNA expression clusters were classified by R packages Mfuzz (v2.50). The KEGG pathway of each cluster was enriched by R packages clusterProfiler (v4.6.2). EPIC structure probed by circSHAPE-MaP was analyzed via CIRCshapemapper v2 (<https://github.com/YangLab/CIRCshapemapper>). The circular RNA secondary structure was modeled by RNAfold(v2.4.2). The 3D structure of EPIC was modeled by 3dRNA (v2.0).

For manuscripts utilizing custom algorithms or software that are central to the research but not yet described in published literature, software must be made available to editors and reviewers. We strongly encourage code deposition in a community repository (e.g. GitHub). See the Nature Portfolio [guidelines for submitting code & software](#) for further information.

Data

Policy information about [availability of data](#)

All manuscripts must include a [data availability statement](#). This statement should provide the following information, where applicable:

- Accession codes, unique identifiers, or web links for publicly available datasets
- A description of any restrictions on data availability
- For clinical datasets or third party data, please ensure that the statement adheres to our [policy](#)

All data supporting the findings of this study is available in the manuscript, Source Data, and at <https://data.mendeley.com/preview/zfm9kmfghs? a=fe43a8b9-6781-424b-92ca-27c2d4a13ed6>. All sequencing data reported in this paper have been deposited in the Gene Expression Omnibus (GEO). High-throughput datasets generated in this study are available at GSE24868077, including circSHAPE-MaP data (GSE248679) and mouse RNA-seq data (IMQ treated Pkr-/- mouse data: GSE248678; mouse spleens delivered EPIC-LNPs data: GSE253346); published RNA-seq data of psoriasis patients was downloaded from GEO under accession number GSE12121278.

Human research participants

Policy information about [studies involving human research participants and Sex and Gender in Research](#).

| | |
|-----------------------------|--|
| Reporting on sex and gender | All four psoriasis patients in Extended Data Fig.10 are male of age ranging from 34 to 59. Gender has no reported impact on psoriasis. pathogenesis (PMID: 23014338). |
| Population characteristics | The four psoriasis patients (age ranging from 34 to 59) were recruited and diagnosed according to Psoriasis Area Severity Index (PASI) score (ranging from 8.3 to 21.2), which has been used for assessing the psoriasis severity in clinical trials. #1: 47 (age), 21.2 (PASI Score) #2: 56 (age), 9.1 (PASI Score) #3: 34 (age), 8.1 (PASI Score) #4: 59(age), 8.3 (PASI Score) |
| Recruitment | Research participants were recruited from volunteer participants through word-of-mouth, active recruitment by study-staff in Beijing Chao-Yang Hospital, Capital Medical University. All recruitment materials were approved by Beijing Chao-Yang Hospital. Advertisements indicated the nature of the study and provide a phone number for further information. |
| Ethics oversight | The study was in compliance with the Declaration of Helsinki and approved by the Research Ethics Board of Beijing Chao-Yang Hospital, Capital Medical University. Written informed consent was signed before the sample collection. |

Note that full information on the approval of the study protocol must also be provided in the manuscript.

Field-specific reporting

Please select the one below that is the best fit for your research. If you are not sure, read the appropriate sections before making your selection.

Life sciences Behavioural & social sciences Ecological, evolutionary & environmental sciences

For a reference copy of the document with all sections, see nature.com/documents/nr-reporting-summary-flat.pdf

Life sciences study design

All studies must disclose on these points even when the disclosure is negative.

| | |
|-----------------|--|
| Sample size | Statistical methods for predetermining sample size was not performed. In each condition reported in the study, we used at least three biological or technical replicates to describe the condition which was a statistically rigorous sample size, to detect differences based on our experience. RNA-seq of mouse samples with different IMQ treatment were performed with 2 repeats (each repeat includes n=2 animals). Total expression level from lesional and non-lesional skin samples derived from 27 psoriasis patients from published data (GSE12121278). EPIC suppressed the expression of psoriatic signature genes in PBMCs isolated from 4 psoriasis patients. |
| Data exclusions | No data was excluded. |
| Replication | In vivo studies were repeated at least three times in independent experiments with similar results. In vitro studies were repeated three times in independent experiments with similar results. All attempts at replication were successful. |
| Randomization | Animals were randomly distributed into cages and randomly chosen for all experiments. |
| Blinding | Our measurements are not subjective. So, there is no requirement for blind experiments. |

Reporting for specific materials, systems and methods

We require information from authors about some types of materials, experimental systems and methods used in many studies. Here, indicate whether each material, system or method listed is relevant to your study. If you are not sure if a list item applies to your research, read the appropriate section before selecting a response.

Materials & experimental systems

| n/a | Involved in the study |
|-------------------------------------|---|
| <input type="checkbox"/> | <input checked="" type="checkbox"/> Antibodies |
| <input type="checkbox"/> | <input checked="" type="checkbox"/> Eukaryotic cell lines |
| <input checked="" type="checkbox"/> | <input type="checkbox"/> Palaeontology and archaeology |
| <input type="checkbox"/> | <input checked="" type="checkbox"/> Animals and other organisms |
| <input checked="" type="checkbox"/> | <input type="checkbox"/> Clinical data |
| <input checked="" type="checkbox"/> | <input type="checkbox"/> Dual use research of concern |

Methods

| n/a | Involved in the study |
|-------------------------------------|---|
| <input checked="" type="checkbox"/> | <input type="checkbox"/> ChIP-seq |
| <input checked="" type="checkbox"/> | <input type="checkbox"/> Flow cytometry |
| <input checked="" type="checkbox"/> | <input type="checkbox"/> MRI-based neuroimaging |

Antibodies

Antibodies used Anti- β -Actin(Sigma, Cat# A3854), Anti-PKR(Abways, Cat# CY5665), PKR Antibody (B-10)(Santa Cruz,Cat# sc-6282), Anti-phospho-PKR (pThr446) (Sigma-Aldrich, Cat#SAB4504517), Anti-eIF2 α (ABclonal, Cat#A0764), Anti-EIF2S1 (phospho S51) (ABCAM, Cat#ab32157) Anti-rabbit-IgG-HRP (Santa Cruz, Cat# sc-2004), Anti-mouse-IgG-HRP(Santa Cruz, Cat# sc-2005)

Validation PKR Antibody (B-10) (1:1,000 dilution), anti-phospho-PKR(pThr446) (1:500 dilution), anti-eIF2 α (ABclonal, 1:500 dilution), anti-EIF2S1(phospho S51)(1:500 dilution),and anti- β -Actin((Sigma, 1:5,000 dilution) were used as described by manufacturer's recommendation for murine western blotting. Anti-PKR(1:2000 dilution) was used for in vitro PKR activation assay.

Eukaryotic cell lines

Policy information about [cell lines and Sex and Gender in Research](#)

| | |
|---|---|
| Cell line source(s) | A549 cell line (SCSP-503) was provided by the Cell Bank, Chinese Academy of Sciences. |
| Authentication | A549 cell line was routinely validated using the Cell Bank (Chinese Academy of Sciences) STR Profiling Cell Authentication Service. |
| Mycoplasma contamination | A549 cell line used was mycoplasma free as tested by the Cell Bank (Chinese Academy of Sciences) |
| Commonly misidentified lines (See ICLAC register) | None was used. |

Animals and other research organisms

Policy information about [studies involving animals; ARRIVE guidelines](#) recommended for reporting animal research, and [Sex and Gender in Research](#)

| | |
|-------------------------|--|
| Laboratory animals | All mice used in this study were on the C57BL/6 background. C ₁ OE mice driven by two different promoters, EF1 α or CAG, were designed in-house and purchased from the Beijing Biocytogen (Beijing, China). Eif2ak2-KO(PKR KO) mice (Strain NO. T015370) were purchased from GemPharmatech (Nanjing, China). Mice were bred and maintained under the specific-pathogen-free condition at the Center for Excellence in Molecular Cell Science (CEMCS), CAS. Mice were used at 6-8 weeks of age. |
| Wild animals | The study did not involve wild animals. |
| Reporting on sex | Unless otherwise stated, male mice were used at 6-8 weeks of age. The experiments conducted in male mice are representative of those in female mice with the same C57BL/6 background (data not shown). |
| Field-collected samples | The study did not involve samples collected from the field. |
| Ethics oversight | The mouse experiments were carried out in accordance with the institutional guidelines and were approved by the Institutional Animal Care and Use Committees at CEMCS, CAS. |

Note that full information on the approval of the study protocol must also be provided in the manuscript.